6 2D Metal Oxides and Their Heterostructures for Gas Chemical Sensing

Katekani Shingange, Steve R. Dima, Modjadji R. Letsoalo, and Eric N. Maluta

6.1 INTRODUCTION

Rapid gas molecule detection at low concentrations is now crucial in a variety of modern applications, including environmental monitoring, interior air quality monitoring, modern farming, food quality monitoring, and medical diagnosis [1–5]. As a result, it has become crucial to develop low-powered, high-performance gas sensors that can identify and track a wide range of gases and vapors, including dangerous and toxic gases and vapors. Typically, gas sensors must adhere to several specifications depending on the applications for which they are designed, including high sensitivity and selectivity, rapid response and recovery, little drift, a low limit of detection, long-term stability, and minimal power consumption [6,7]. A variety of sensing technologies have been developed over the past few decades based on various underlying signal transduction mechanisms, such as electrochemical [8,9], thermoelectric [10,11], calorimetric [12,13], and optical devices [14], to address the challenges of low-concentration and quick detection of gas molecules. Among them, electrically transduced devices have drawn a lot of attention due to their ease of use, low cost, ability to monitor signals in real-time, ability to be miniaturized, and compatibility with other common electronic devices [6,15].

To create gas sensors, a range of materials have been investigated, including metal oxides (MOXs) [16,17], carbon nanomaterials [18–20], and conducting polymers [21,22]. Among them, MOXs provide highly accurate, affordable target gas molecule detection. As much as MOXs are an interesting choice of sensing layer material for gas sensors, these materials suffer from a lack of selectivity and high-temperature operation [23]. To address this, researchers have been on a quest to search for innovative gas sensing materials or structures with improved sensitivity and selectivity for operation at low temperatures, preferably room temperature (RT). It has been established that structure dimensions (0D, 1D, 2D, or 3D) of MOX materials can influence the gas sensing performance of the MOX materials [24–28]. The inimitable physical and chemical properties of 2D nanostructured MOX materials, which have lateral dimensions up to several centimeters and thicknesses ranging from a few to tens of nanometers, make them excellent candidates for electrically transducing chemical gas sensors [29–31].

2D MOXs can be split into three groups according to their crystal structure, i.e., layered, lamellar, and non-layered. Layered MOXs include materials assembled from M-O (M: Mn, Mo, or V) octahedral, whereby the in-plane atoms are joined by strong chemical bonding, and the stacking layers are combined by weak van der Waals (vdW) interface [32,33]. Different oxides from Al, Co, Cu, Fe, Gd, Ge, Mn, Ni, and Ti also possess a layered crystal structure with unique planar hexagonal coordination, which is different from their conventional non-polarized crystal structures seen at room temperature [34]. Most ultrathin 2D MOXs do not have a layered crystal structure because all atoms are bound by strong chemical bonds, leading to abundant unsaturated bonds on surfaces or edges, resulting in high-activity and high-energy surfaces such as

DOI: 10.1201/9781003436942-6

ZnO, In_2O_3, WO_3, and TiO_2 [35]. Furthermore, it should be noted that the lamellar MOX consisting of foreign ions incorporated into the atomic layer gaps has also attracted extensive research, of which Perovskite is a typical example [36,37].

MOX-based sensors function based on the well-known resistance change mechanism, which involves adsorption–desorption processes and catalytic reactions occurring on the surface of the MOX, followed by an electronic exchange between adsorbed molecules and the bulk of MOX. A change in resistance/conduction of the MOX sensing layer follows as a result of these reactions, which is proportional to the concentration of the test gas. Plenty of reports for both n- and p-type MOX sensing mechanisms in reducing or oxidizing gases at different environmental conditions have been reported before [38–43]. Normally, surface oxygen species are recognized as active sites that play an important role in the gas sensing process [43]. Oxygen species absorbed on the surface of metal oxides can react with the target molecules, release electrons, and conduct an interfacial redox reaction, resulting in higher oxygen vacancies [44]. However, these MOX gas sensing reactions are not only dependent on the number of oxygen vacancies, but also highly dependent on their local environment, especially the symmetry of oxygen vacancies [45].

Despite considerable progress in the use of 2D MOXs as sensing materials, they still suffer from some inherent limitations. The ability of 2D heterostructures constructed from vdW stacking of 2D vertical heterostructures or edge covalent bonds of 2D lateral heterostructures has proven to not only solve the lack of performance problems of a single 2D MOX-based materials in chemical gas sensors, but also to generate many unique properties through the synergistic advantages of individual 2D MOX-based materials. The selected MOX materials ultimately determine the principles of gas adsorption, reaction, and electrical structure.

Heterostructures are manufactured by integrating the p-type and n-type MOXs, which can combine various properties of the individual materials into a single system. On a microscopic scale, the physical interface between two different materials is called heterojunction. Heterostructures offer combined effects of increased surface reactivity through catalysis/adsorption and charge transfer between heterojunctions, which leads to better gas sensing performance. It is well known from solid-state physics that by contacting two different semiconductor materials at the interface, the Fermi level reaches the same energy, which often leads to charge transfer and depletion layer formation. Although this depletion zone is one of the most notable effects, many other factors may be responsible for improving the gas detection performance of these heterostructures-based gas sensors.

The work in this chapter is structured to discuss current advances in the development of chemical gas sensors using 2D MOX nanostructures and their heterostructures. Within this chapter, we will present an insight into the achievements and limitations of 2D MOX in the field of chemical gas sensors focusing on selected 2D. Experimental and computational perspectives will be used to understand the sensing performance of the 2D MOX-based chemical gas sensors and their functional characteristics. We will first touch on the fundamentals of 2D MOXs, then discuss different types of MOXs and their gas sensing performance looking at both experimental and computational perspectives.

6.2 BASICS OF 2D METAL OXIDES

Based on structural characteristics, 2D MOXs are divided into three categories: layer, lamellar, and non-layer MOXs. The layered MOXs include the traditional layered MOXs (e.g., MoO_3 and V_2O_5), emerging hexagonal MOXs (e.g., TiO_2 and Ni_2O_3), and layered double hydroxides (LDHs). As an example of the traditional layered MOXs, Figure 6.1 shows the structure of MoO_3 displaying a layered structure in which each layer is largely composed of distorted MoO_6 octahedral in an orthorhombic crystal [46].

Layered planar hexagonal MOX includes mono- and few-layered hexagonal, such as TiO_2 and Ni_2O_3 derived from the metal–gas interface [34]. Each atomic layer is composed of a hexagonal

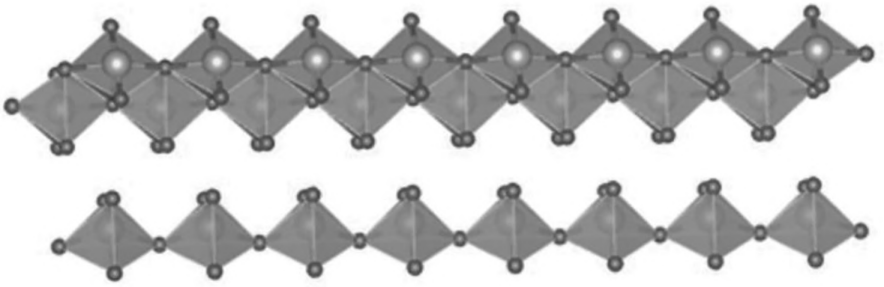

FIGURE 6.1 Crystalline structure of MoO_3. (Produced using software provided by Ref. [47].)

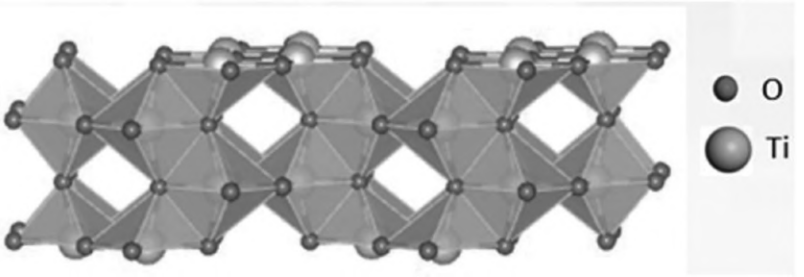

FIGURE 6.2 Crystalline structure of TiO_2. (Produced using software provided by Ref. [47].)

ring that accommodates both the metal and oxygen atoms [48]. Figure 6.2 depicts the crystalline structure of TiO_2 as an example of the layered planar hexagonal MOX.

LDHs are structurally conformed by a consecutive repetition of individual sheets located in parallel spatial planes that are electrostatically bonded by vdW interactions or hydrogen bonds along the perpendicular plane [49]. A schematic interpretation of the LDH structure is displayed in Figure 6.3, which reveals the LDH configuration comprised of stacked lamellas. The chemical composition of LDH materials can be expressed by the following general formula [49]:

$$[M^{2+}_{1-x}M^{3+}_{x}(OH)_2]_x[A^{n-}]_{x/n}zH_2O$$

where $M^{2+}$and M^{3+} are two metals, M^{2+} can be Mg^{2+}, Ni^{2+}, or Zn^{2+} and M^{3+} can be Al^{3+}, Mn^{3+}, Ga^{3+}, and Fe^{3+}, and A^{n-} is an anion such as Cl^-, CO_3^{2-}, SO_4^{2-}, or RCO_2^-, and x is usually between 0.2 and 0 [49]. LDHs have a lattice structure formed by stacking positively charged brucite-shaped layers, consisting of a divalent metal ion M^{2+} octahedrally surrounded by six $(OH)^-$hydroxyl groups. The substitution of the M^{2+} metal with a trivalent M^{3+} cation gives rise to the periodic repetition of positively charged sheets (lamellas) alternating with charge-counterbalancing A^{n-} ions that allow the electrostatic neutrality of the brucite layers. This charge displacement produces the possibility of dipole–dipole interactions onto the lamella surfaces, enabling interaction with anions or molecules possessing an electrical dipole. Moreover, inside the interlayer space, water molecules are generally accommodated, and a network of hydrogen bonds is present among layers, providing also interacting sites for external molecules. The possibility of intercalating different anions in LDH structure has been largely demonstrated [50], and the possibilities of modifying the chemical, electronic, or optic properties of LDH by changing the anion [51]. In this way, at least in principle, the relative response to various volatile compounds could be tuned by means of anion substitution. LDHs possess a large surface-to-volume ratio and LDH structures can adsorb any kind of molecule [52], making them applicable for chemical gas sensing.

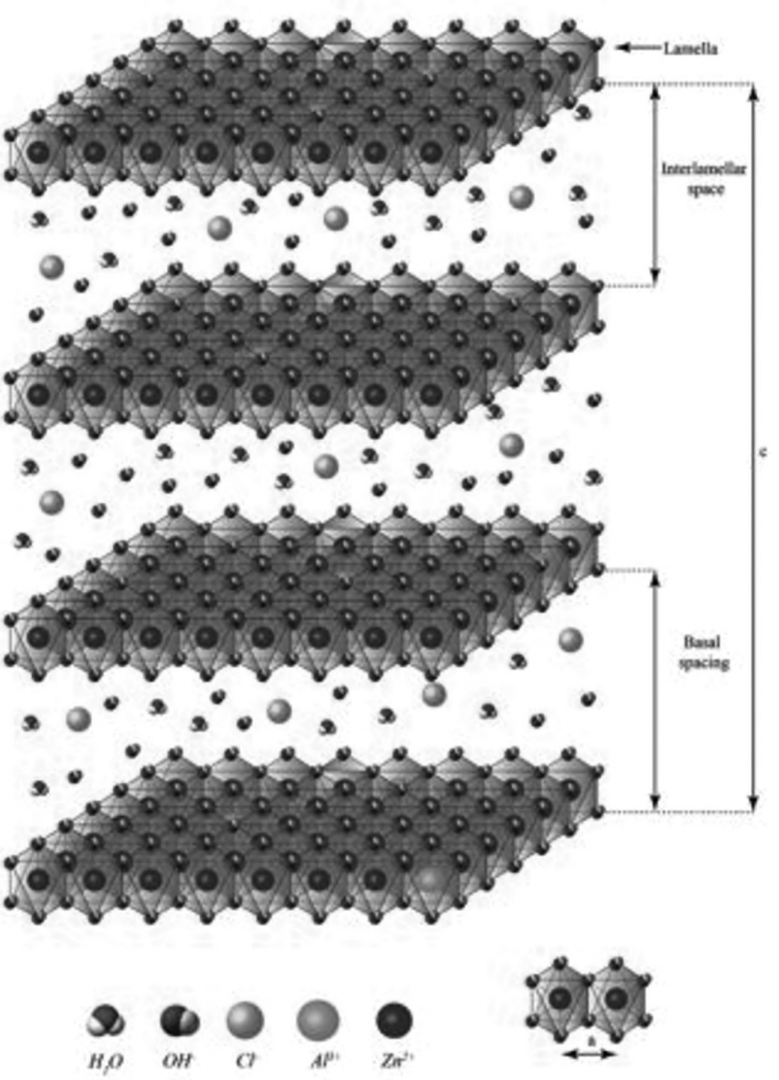

FIGURE 6.3 LDH general structure. (Reproduced with permission from Ref. [53], Copyright © 2017 Elsevier.)

In the lamellar MOXs, atoms or ions are bonded to the oxide layer by weak electrostatic forces. For instance, perovskite $CaTiO_3$ (Figure 6.4) consists of corner-linked TiO_6 octahedra with Ca atoms distributed between the octahedral [54]. At high temperatures, the crystal structure is cubic, but at room temperature, the crystal structure is orthorhombic, with a space group of Pbnm and a Glazer octahedral tilt system of a−a−c+ [55].

The fineness of the atomic scale gives 2D MOX interesting properties such as optical transparency and mechanical flexibility, which can be used in flexible electronics and new optical electronics. Other advantages include high theoretical capacitance, large surface area, and the possibility of oxidation–reduction reactions, making 2D MOX ideal for high-density supercapacitors and batteries [56,57]. Furthermore, their excellent photoelectric properties and high surface chemical reactivity make them suitable for their use as photocatalysts and gas and biosensors [58,59].

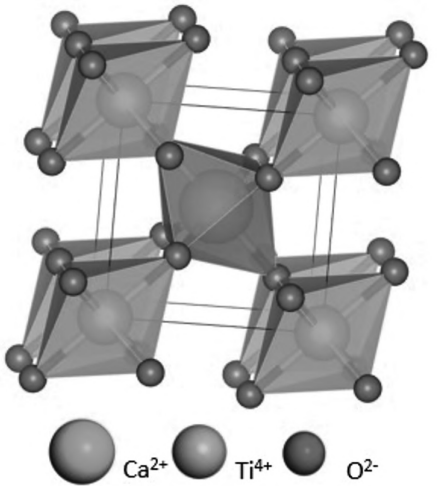

FIGURE 6.4 Crystalline structure of $CaTiO_3$. (Produced using software provided by Ref. [47].)

6.3 THE APPEAL BEHIND 2D METAL OXIDES APPLICATIONS

For MOX-based sensing materials, the morphology influences gas sensing performance as structure dimension (1D, 2D, or 3D) and size affect the material's characteristics, which then influence the sensing performance of the sensing material. 2D MOX nanostructures exhibit a notably greater specific surface area in comparison to their other 0D, 1D, and 3D counterparts. In addition, the gas sensing layers possess distinctive material characteristics due to dimensional confinement, such as the ability to manipulate electrical properties and visible light absorption through quantum size effects that adjust the band gap [60]. Moreover, the mechanical durability and pliability of 2D MOX enable their integration with flexible substrates, exhibiting a high degree of compatibility and facilitating the exploration of novel applications, such as wearable chemical sensors [61,62].

Over the past decade, there has been notable advancement in the fabrication of 2D MOXs ranging from nanosheets, platelets, etc., which have led to a better understanding of the principles behind their engineered synthesis [58,63–65]. This has also resulted in their increased utilization as chemical gas sensing layers. The simplest method is to obtain these 2D MOX structures using various exfoliation techniques from their parent layers, making them different from other low-dimensional nanostructure materials whose synthesis is heavily dependent on crystalline growth.

The thickness of these 2D layers corresponds to the crystal thickness of the individual layer, usually less than 5 nm. The side crystal size of layers of materials along the plane direction remains unchanged, leading to high morphological anisotropy of thickness of sub-nanometer and side dimension up to micrometer. Because the surface-to-volume ratio is close to one, these 2D MOX structures practically expose all components to the surface. This allows the hydrophilic, hydrophobic, surface charge, and surface structure to be adjusted as required for applications [66]. Similarly, there are other techniques such as the top-down approach of soft chemical exfoliation methods that are equally efficient in obtaining 2D MOX structures. In the absence of interlayer interactions and low dimensions, overlaps are observed, improving the surface properties and surface instability of these structures. The description of the structure and properties of any material is essential to understand the resulting behavior and design of unconventional functional materials. This was made possible in recent years by the increase in the capability of the calculation of the First Principle. Similarly, Density Functional Theory (DFT) is widely used to study

the intriguing properties of bulk and 2D MOX. However, when working with oxides in 2D form, unique properties begin to develop due to the presence of a large surface area and oxygen atoms on the surface, which leads to significant changes in surface energy that enhance the properties of the material.

The basic atomic structure of MOX determines the nature of conductivity, non-conductivity, and semi-conductivity. The relatively small thickness of 2D material influenced the quantum confinement effect and its effects on electron band structure, charge transport, and optical properties. Due to technological miniaturization, increasing surface is the current need. Consequently, nanostructure MOXs were created by reducing their size to a few nanometers. This change has led to several technological developments toward the development of 2D ultra-thin structures derived from their bulk forms, with significant changes in structure and phase, and improved physiological chemistry properties such as better surface of adsorbents, tuned electronic band structures, and improved photocatalytic behavior.

The predominant avenue of research in the field of gas sensing mechanisms for 2D MOX-based materials pertains to the adsorption of gas molecules. This adsorption may take the form of physisorption or chemisorption, and it is often analyzed through the lens of charge transfer theory. The adsorption of target gases on the surface of 2D MOX-based materials typically results in modifications to the resistance and carrier concentration. In general, 2D MOX materials demonstrate physisorption to gas molecules with relatively low binding energy because of vdW interactions. In the context of chemisorption, the increased binding energy of gas molecules is attributed to the charge transfer mechanism that occurs between the sensing material and the gas molecules. As a result, the recovery process for chemisorption is comparatively prolonged in comparison to physisorption.

It is widely recognized that 2D MOX-based materials exhibit either donor or acceptor behavior toward specific gas molecules. In the context of 2D MOX-based materials, if the Fermi level is situated below the highest occupied molecular orbital (HOMO) state of the adsorbate gas molecules, a phenomenon of charge transfer from the adsorbate to the 2D MOX nanomaterials takes place. This results in an upshift of the Fermi level of the 2D MOX-based materials. In contrast, when the Fermi level of 2D MOX-based materials surpasses the lowest unoccupied molecular orbital (LUMO) state, there is a transfer of charge from the 2D MOX-based materials to the adsorbate, resulting in a reduction of the Fermi level of the 2D MOX-based materials.

The utilization of DFT calculations is feasible for the evaluation of the complete charges transferred and the binding energy that exists between adsorbate and 2D MOX-based materials [67]. In addition, DFT calculations facilitate the determination of the sensing response that occurs when adsorbate and gas molecules interact, based on the calculated total charge and binding energy. It is noteworthy that chemisorption and physisorption can be distinguished by the respective indications of high binding energy and low binding energy [67]. Consequently, it is feasible to anticipate the gas sensing characteristics, such as sensitivity and selectivity toward gas molecules, for the surface of 2D MOX-based materials.

In this section, we will give an overview of current advancements in a variety of chemical gas sensing performances of 2D MOX-based materials in their respective classes, coupled with DFT calculations used to understand the gas molecules' interactions with the surface of the materials. We also compare each of their advantages and weaknesses, placing more emphasis on the overall gas sensor performances to determine the future research directions for better gas sensor performance.

6.4 GAS CHEMICAL SENSING WITH 2D METAL OXIDES

Nanostructured 2D MOX materials including nanoplates, nanosheets, and nanoflakes have advantageous characteristics that cannot be achieved by traditional bulk materials. These characteristics include high surface area and high-surface-to-volume ratio, providing more active sites for gas adsorption, chemisorption, and catalytic activities that control the gas sensing performance. Additionally, for 2D MOX, only one or two crystallographic planes are involved in the sensing

performance, thus simplifying the modeling of processes taking place on the MOX sensing material surface, contributing to a better understanding of the influence of sensing performance, and allowing for ways to manipulate better selectivity of the material [68]. Theoretical and experimental results indicate that nanostructured materials with exposed crystal surfaces can exhibit special features in gas sensor applications [27,69,70]. For example, Su et al. [71] fabricated single crystal copper oxide nanoplatelets with a high percentage of {001} facets by a hydrothermal method. X-ray diffraction, Fourier transform infrared spectroscopy, field emission scanning electron microscopy, and high-resolution transmission microscopy were used to characterize the as-prepared materials. From the DFT calculations, it was determined that the {001} facets have the highest surface energy. Due to that, the CuO nanoplatelets revealed high sensing responses to ethanol, acetone, butanol, and isopropanol. In another work by Xue et al. [72], they demonstrated that ZnO nanodishes with exposed (0001) crystal facet sensor exhibited the best response of 49–100 ppm ethanol at 230°C among four as-synthesized samples, while non-customized ZnO was only 28.

Most 2D MOXs have high surface areas and porous structures that provide more gas diffusion channels and more active areas for sensor reactions. Therefore, porous structures improve MOX gas detection properties. Defects in crystal structures, including interstitial and vacancy defects, usually occur in MOXs. In addition to porous structures and high surface areas, surface defects are also considered to be an important factor in MOX gas sensitivity performance. For example, Liu et al. [73] prepared porous ZnO ultrathin nanosheets for the detection of acetylacetone. Their findings revealed that porous ZnO ultrathin nanosheets had excellent selectivity and operational stability, with a response four times higher than the ZnO clusters. They attributed the excellent sensing performance to the high specific surface area and ample surface oxygen vacancy. In another study by Xue et al. [72], the influence of oxygen vacancy (V_O) and zinc interstitial (Zn_i) on the ethanol sensing performance was investigated. The results demonstrated that the ZnO sensor with rich electron donor surface defects Zn_i and V_O displayed greater ethanol gas sensing. These results confirm that surface defects are advantageous for the gas sensing property of MOXs.

Although the advantages of 2D MOX-based materials are interesting, these materials still have some shortcomings when applied in gas sensing. It is difficult to fabricate large and thin 2D MOX nanomaterials using the normal MOX synthesis methods. For a sensor to be able to give a high response, the thickness of the 2D MOX nanostructured material should be comparable with the Debye length (2–5 nm) [39,74,75]; however, this is not the case for 2D MOX materials obtained from traditional synthesis methods; the 2D MOX nanostructured materials are found to be more than 30–50 nm, thus limiting sensitivity. Also, stacking of the 2D MOX nanostructured materials can result in the formation of a denser arrangement, which can hinder gas penetration into the inner voids of the 2D structures, thus decreasing the sensitivity [76]. Therefore, the synthesis of 2D MOX structures must be advanced to be able to yield ultrathin 2D MOXs to maximize their capabilities in gas sensing.

The following sections will discuss different 2D MOX-based materials in detail, as well as their applications in gas sensing, looking at selected examples of 2D-based MOX nanomaterials.

6.5 PREPARATION STRATEGIES OF 2D METAL OXIDES

In general, 2D MOX-based materials are prepared using traditional top-down and bottom-up methods. The top-down synthesis method involves intercalation and exfoliation of bulk-layer MOX in single-layer or few-layer 2D MOX [77]. Bottom-up approaches are a direct growth process that can control the substrate and thickness of desired materials. Wet chemical synthesis, a surfactant-led approach, and self-assembly methods are used in the bottom-up approach [56,78]. In addition, hydrothermal chemical methods can be used to synthesize 2D MOX, with greater yields, easier processing and control, and less energy waste [79,80].

Sun et al. [81] reported a comprehensive and fundamental methodology for the molecular self-assembly synthesis of ultrathin 2D nanosheets of MOXs, such as ZnO, Co_3O_4, and WO_3.

In their work, they proposed a methodology for the surfactant self-assembly of ultrathin 2D MOX nanosheets. The approach involved the formation of inverse lamellar micelles comprising polyethylene oxide–polypropylene oxide–polyethylene oxide (PEO20–PPO70–PEO20, Pluronic P123) surfactant and ethylene glycol (EG) co-surfactant in an ethanol solvent. The molecular assembly process of ultrathin 2D MOX nanosheets from liquid solutions involves the strategic and collaborative self-assembly of MOX precursor oligomers into lamellar structures with the assistance of polymer surfactant molecules. Subsequently, these structures undergo condensation, polymerization, and crystallization to form 2D MOX nanosheets. The synthesized crystallized ultrathin 2D MOX nanosheets were observed to possess limited thickness, a substantial specific surface area, and chemically reactive facets. The UV–vis adsorption spectra of TiO_2, ZnO, Co_3O_4, and WO_3 nanosheets exhibited a blue shift in comparison to their bulk counterparts, indicating a pronounced quantum confinement effect in the thinnest dimension. The phenomenon known as the quantum size effect is observed when the conduction band is raised and the valence band is lowered due to the reduced size of MOX nanoparticles. This is commonly understood to result in a blue shift in the absorption edge.

Different synthesis techniques yield different structures with different functional properties, and therefore, it is important to find or design a synthesis technique that can yield the best characteristics for the application. For gas sensing applications, it would be great to design a synthesis method that can yield materials with high surface area and high carrier mobility. In the following section, the synthesis methods and chemical gas sensing performance of the various MOXs will be discussed.

6.6 GAS SENSING PERFORMANCE

It is important to compare and systematically select the synthesis method according to the type of application. Different methods have different advantages and disadvantages for preparing 2D MOXs. Therefore, it is necessary to choose the method based on its advantages and disadvantages. The following is a discussion on studies for the gas sensing performance applying different 2D MOXs with an emphasis on their methods of fabrication and characteristics correlated with their sensing performance. The experimental and computational perspectives will be considered in the discussion.

6.6.1 Traditional Metal Oxides

Traditional MOXs such as semiconducting metal oxides ZnO [82,83], SnO_2 [84,85], TiO_2 [41,86], CuO [87], and NiO [88] have been extensively studied for chemical gas sensing applications. Particularly in 2D format, traditional MOXs have been synthesized through different techniques. These 2D MOXs have seen applications for the detection of several gases such as NO_2, NH_3, and H_2S [58,89]. Gas sensing mechanisms are known to be based on resistance changes in sensing materials caused by surface oxygen species and target gases. The amount of oxygen adsorbed on the surface is directly affected by the particle size, shape, surface area, surface defects, and interface properties of the sensor material. All these characteristics rely on the method of obtaining the sensing material. For these MOXs, usually the n-type such as ZnO and SnO_2 are favored in contrast to their p-type such as CuO and NiO; this is because even in the same conformations, for instance, rod-shape, the response in p-type MOXs is nearly the square root of the response in n-type [90].

As one of the popular traditional MOXs explored for chemical gas sensing, ZnO is one of the important wide band gap, n-type MOX that is mostly used for chemical gas sensing applications. 2D ZnO structures have been shown to be sensitive to a variety of gases under different conditions. For example, Zhang et al. [91] employed a hydrothermal method to synthesize porous 2D ZnO single-crystal nanosheets with hexagonal wurtzite and mesoporous structures. This was achieved by synthesizing zinc carbonate hydroxide hydrate precursors at a low temperature of 80°C in an

environment-friendly hydrothermal method that did not include the use of any surfactant or organic solvent, followed by annealing at 300°C for 0.5 h in an air environment. The ZnO nanosheets-based gas sensor unveiled notable sensitivity and rapid response and recovery times when detecting ethanol concentrations within the range of 0.01–1000 ppm. The sensor also demonstrated a low detection limit of 10 ppb ($R_a/R_g = 3.05$), as well as exceptional selectivity and stability at 400°C. The high ethanol response of the ZnO nanosheets-based sensor was attributed to its large specific surface area, single-crystal structure, plane-contact between nanosheets, and the small thickness (10–40 nm thickness). These findings suggest that these nanosheets are highly suitable for the development of ethanol sensors with practical applications.

Oosthuizen et al. [92] used a sonochemical method for the synthesis of p-type CuO nanoplates by the transformation of copper nitrate solution under basic aqueous conditions into CuO nanoplatelets and flower-like nanostructures, without the assistance of any surfactants and additives. Their study demonstrated the effects of reaction time on the diameter of the CuO nanostructured materials, whereby the diameter was found to decrease with increasing reaction time. They also observed that, under the same reaction condition, the modification of the $[Cu(H_2O)_6]^{2+}$ ion complex to $[Cu(NH_3)_4(H_2O)_2]^{2+}$ ion complex, before the addition of NaOH as a base, allowed the surface morphology to change from nanoplatelets to flower-like nanostructures. The as-prepared CuO nanoplatelets were comprehensively characterized in detail using X-ray diffraction, scanning electron microscopy, transmission electron microscopy, Raman spectroscopy, photoluminescence spectroscopy, and Brunauer–Emmett–Teller (BET) surface area analyses. The structural analyses disclosed a size-dependent broadening due to the decrease in platelet size as the reaction temperature was increased. From PL studies, it was observed that the CuO nanostructures displayed several emissions, which were attributed due to various sizes and shapes of CuO nanoplatelets, suggesting that the luminescence property of CuO is dependent on the morphology of the nanomaterials. They further performed a study on the gas sensing performance of the CuO nanoplatelets toward various gases, including CH_4, CO, H_2S, NH_3, and NO_2. Their findings revealed that the surface area, sensing response, and point defects are dependent on the synthesis reaction temperature.

The sensing capabilities of the asymmetric 2D Ga_2O_3 monolayer were examined by Zhao et al. [93], who conducted a study on the adsorption properties of six harmful inorganic gas molecules namely CO, NO, NO_2, NH_3, H_2S, and SO_2, as well as three common ambient molecules namely O_2, CO_2, and H_2O using DFT calculations. The findings indicated that significant variations in adsorption between the upper and lower surfaces were observed due to the inherent internal electric field. The 2D Ga_2O_3 monolayer exhibited distinctive adsorption properties for NO gas molecules. The computed results pertaining to the transport properties of Ga_2O_3 MOSFETs indicated their potential as a viable and recyclable sensor for detecting NO gas. Also, it has been seen that using biaxial strain engineering on a single layer of 2D Ga_2O_3 can make it possible to get gas sensing capabilities that can be changed.

The study conducted by Li et al. [94] utilized DFT computations to examine the adsorption of ten gaseous molecules namely O_2, N_2, NH_3, NO, CO, CO_2, CH_4, C_2H_6, HCHO, and H_2S on three distinct 2D WO_3 nanolayers. They employed a non-equilibrium green function (NEGF) methodology to accurately evaluate the electron transport characteristics, which is a crucial aspect of gas detection. The study's findings also indicated that the 2D WO_3 nanolayers exhibited notable sensitivity and selectivity toward NH_3, NO, HCHO, O_2, and H_2S. The analysis of transport properties, specifically transmission functions and current–voltage (I–V) characteristics, suggested that the electronic device characteristics (ON and OFF) of gas sensors can be effectively achieved through the presence or absence of gas molecules on the 2D WO_3 nanolayers. The binding energies computed indicated that the intermolecular interactions between the gas molecules and 2D WO_3 nanolayers, which were extracted from the (0 0 1) plane of WO_3 bulk crystal, exhibited greater strength compared to those with certain other 2D materials such as graphene and borophene.

6.6.2 Layered Double Hydroxides: Synthesis and Sensing Performance

In recent years, LDHs have been explored for gas sensor applications. This class of materials has attracted attention in the field of gas sensors due to their inherent characteristics such as hierarchical structure, significantly higher stability over a prolonged period, compositional flexibility, anion exchangeability, and a large specific surface that is useful for rapid gas adsorption and desorption [95,96]. LDHs contain anions (e.g., CO_3^{2-} and Cl^-), intercalated between positive layers, which significantly affect their structure. By varying the metallic cations, their ratio, and the interlayer anions, a great number of LDH types can be formed. LDHs structure exhibits a pathway facilitating carrier diffusion; therefore, they received considerable attention for direct potential applications in gas sensors for monitoring a wide class of gases and vapors [42]. Numerous studies related to the synthesis of LDH-based materials have discussed simple and inexpensive methods for synthesis in the laboratory and on an industrial scale [42]. Materials obtained from Pt/Zn/Al LDHs were the first attempts to use LDHs gas sensors whereby changes in the absorbance of all the samples before and after reducing treatments were studied by FT-IR spectra [97]. They reported that due to their memory effect, after calcination, LDHs do not lose their network structure and are able to rebuild it, and this happens after rehydration. Also, the initial structure of LDH does not change after calcination and does not lose its specific surface area. Polese et al. [53] synthesized chlorine-intercalated Zn-Al-LDH and used it for the detection of five volatile compounds, i.e., CO, CO_2, NO, NO_2, and CH_4 at concentrations of 25, 62, 100, 125, 162, and 250 ppm per gas at room temperature (~ 22°C). Each concentration was obtained by diluting in nitrogen CO, CO_2, NO, NO_2, and CH_4 concentrations measured from certified bottles. The sensors were exposed for 60 s to six gas concentrations and then cleaned in wet nitrogen for 500 s. During the entire measurements, the humidity was kept constant at 50% relative humidity (RH) fluxing 100 standard cubic centimeter (sccm) of pure nitrogen through a gas bubbler containing deionized water. The RH level was maintained constant to avoid possible changes in the LDH interlamellar content of water. Finally, every volatile compound was measured in triplicate at room temperature, and the DC sensor resistances were measured by means of an Agilent 34401a multimeter connected to a PC. Under the applied conditions, the LDHs-based sensors showed the ability to differentiate several concentrations with very good short-term stability. The ability of these LDH structures to detect various pollutant volatile compounds at room temperature without the requirements of a heating element is quite interesting in the sensors field as this suggests that the sensors will not require power to operate, thus they are energy-saving. Since this work was one of the very first works on LDHs as sensing materials, the mechanism behind the response could not be fully concluded.

Shinde et al. [30] synthesized a self-assembled Zn-Cr-WO interconnected sheet-like LDH structure to detect gas Cl_2 at room temperature. Exfoliation-restacking-based intercalative hybridization routes have been used to introduce foreign species of polyoxotungstate (POW) in the Zn-Cr-LDH grid, which has led to crucial changes in the chemical composition of host LDH materials. Compared to the original Zn-Cr-LDH, the resulting self-assembled Zn-Cr-WO displayed improved surface characteristics, extended base spacing, and micromesoporous structure. The Zn-Cr-WO sensors were studied at room temperature for various oxidizing and reducing gases, i.e., NO_2, Cl_2, LPG, H_2, H_2S, CO, and NH_3. The selectivity results showed that the Zn-Cr-WO sensor was significantly selective to Cl_2 compared to other interference gases. The lowest POW content of Zn-Cr-WO-1 nanohybrid (Zn-Cr-LDH/POW = 0.66) had excellent dynamic response recovery characteristics, with a gas detection limit of 0.1 ppm and a 66.6% response rate to Cl_2. Compared to a variety of Cl_2 sensors such as SnO_2, ZnO, In_2O_3, WO_3, and SWCNT, the LDH-based sensors have shown a lot of promising functions in gas sensor applications, with excellent sensing responses and superior room temperature repeatability [30]. They attributed the great Cl_2 sensing performance to the unique interconnected sheets-like mesoporous microstructure, which facilitated excellent permeability for gas adsorption. The structure also provided enhanced surface area with active surface sites for chemical interaction. Additionally, with expanded interlamellar spacing of 0.73 nm due to

the intercalation of foreign POW fractions, Zn-Cr-WO-1 exhibited wider mesopore channels that continuously accelerated the gas molecules adsorption in the inter-gallery space between laminated LDH nanosheets [30]. LDHs have unique physicochemical properties such as high surface area and high porosity, anion and cation exchange capacity, and adjustable structure engineering with high controllability. LDHs have drawbacks including agglomeration and low conductivity, which make their use in gas sensing limited.

6.6.3 Perovskites Oxides: Synthesis and Sensing Performance

Another family of MOX with layered 2D structures is the Perovskites family with a general formula of ABO_3, with A and B cations of different sizes [98]. Perovskites consist of three types of layered phases, which are the Aurivillius (AU) with general formula $[Bi_2O_2]$-$[A_{(n-1)}B_nO_{3n+1}]$, Dion-Jacobson (DJ) with general formula $MA_{(n-1)}B_nO_{(3n+1)}$, and Ruddlesden–Popper (RP) with general formula $A_{n+1}B_nX_{3n+1}$ [99]. In the Ruddlesden–Popper Perovskite (RPP), R is a long chain alkyl or aromatic group that acts as a spacer covering the perovskite layer, and because of isolation, the moister resistibility increases. The number of perovskite layers between spacers is denoted as n [100]. 2D MOX perovskites have several advantages, including air, phase, and thermal stability. Improvements in air stability in 2D perovskites are associated with vdW interactions of capping agent molecules [100].

Despite the superiority of 2D MOX perovskites, the quantum confinement effect increases the band gap of 2D MOX perovskites compared to other dimensions. Furthermore, due to the isolation characteristics of organic space cations, 2D MOX perovskites exhibit high-sensitivity transportation behavior, high inorganic conductivity, and low layers. The physical characteristics of 2D or almost 2D perovskite materials are determined primarily by the bulky organic cations present in the system. These cations play a crucial role in defining the dimensionality and phase behavior of the material, as demonstrated in the studies conducted by Saparov et al. [101]. The electronic characteristics of the resulting materials are solely determined by the properties of the inorganic layers due to the substantial HOMO/LUMO gap exhibited by these organic cations. Maheshwari et al. [102] employed DFT calculations to demonstrate that the incorporation of electron-withdrawing and electron-donating molecules results in the creation of localized states, which can be observed in either the organic or inorganic component. Additionally, it has been demonstrated that the energy levels of the bands located in the organic and inorganic components can be adjusted separately. Modulation of organic cation levels can be achieved through alterations in the electron-withdrawing or -donating properties, while the manipulation of energy levels in the inorganic component can be accomplished by adjusting the number of inorganic perovskite layers.

Recently, various perovskite-based sensors have been reported to detect several gases such as NH_3 [103,104], NO_2 [105], and O_2 [106] and humidity [107]. When a film is exposed to gas/vapor, the gas/vapor can fill the gaps in the film, thereby significantly increasing the film's conductivity. In contrast, when inert gas/vapors reach the perovskite film, the inert gas/vapor molecules remove the target gas/vapor molecules and increase the number of vacancies, thereby reducing the conductivity of the perovskite film [105,107]. Although 3D perovskites have made significant advances in device efficiency, due to their poor stability in water, oxygen, heat, and continuous light exposure, their optical and long-term stability is limited [105,106,108,109]. On the other hand, 2D perovskites are more interesting because of their good stability, unique structure, and excellent optical and electron characteristics [110]. Different findings have previously been reported highlighting the potential for the use of 2D perovskites to produce gas sensors, such as those by Tien et al. [111], whereby they compared 2D-$(PEA)_2PbBr_4$ perovskite with 3D-$MAPbBr_3$ perovskite. They found that the horizontal vapor sensor of 2D-$(PEA)_2PbBr_4$ perovskite was much superior to 3D-$MAPbBr_3$. They attributed high responses to a large ratio of surface to volume and showed a 2D transverse perovskite layer suitable for ethanol detection. Another study by Wang et al. [37] reported on the comparison of 2D $NbMoO_6$, $NbWO_6$, $TaWO_6$, and $TaMoO_6$ nanosheets synthesized through liquid exfoliation and their gas sensing performance toward H_2S and other

small molecules of volatile gases. The gas sensor performance toward 5–500 ppm H_2S revealed that, among the four perovskites with similar structures, nanosheets made from n-type $NbWO_6$ showed high sensitivity to H_2S, with response and recovery time of 6 and 30 s at 50 ppm H_2S at a low operating temperature of 150°C. The H_2S sensor performance of the 2D $NbWO_6$ perovskite was attributed to the high surface areas with nearly fully exposed active sites, which significantly facilitated the H_2S gas molecules adsorption–desorption, diffusion, and transmission for high selectivity under low operating temperature. Another reason was the high crystalline framework of the 2D $NbWO_6$ nanosheets that promoted fast transport of electrons between surface and bulk for significantly enhanced response and response dynamics and sensitivity. The electronic transfer associated with the gas sensing process was further explained using the DFT calculations. The DOS of the $NbWO_{6+}H_2S$ showed a new energy level in the conduction band and the band gap was narrowed, which was attributed to the strong bonding adsorption of H_2S on the $NbWO_6$ nanosheets, which decreased the resistance for high selectivity and sensitivity. The adsorption configurations of the (110) plane on the $NbWO_6$ nanosheets were optimized, and no obvious changes in configurations were observed after the adsorption of gas molecules onto the $NbWO_6$ nanosheets. These $NbWO_6$ nanosheets could find application for fast and effective detection of H_2S, especially for the environmental standard set threshold of H_2S which is at 0.1–100 ppm [112].

6.7 HETEROSTRUCTURES OF 2D METAL OXIDES

By growing 2D MOXs monolayers and restacking them into blends with 0D, 1D, 3D, or other 2D nanostructures, different types of heterostructures can be created. Together with the ability to overcome the immanent restrictions of each component material, the many ways that 2D MOX nanostructures can be mixed with other materials create new opportunities to create devices configurations with a flexible electronic property that goes beyond a single material's scope [113,114].

Due to their intriguing features that are absent from bulk semiconductor heterojunction devices, heterostructures of layered 2D MOX nanostructured materials show outstanding potential for applications in many fields. Initial attempts to combine 2D layered nanomaterials with 0D and 1D nanostructures have opened a new area of nanoscale material integration and opportunities to develop new applications for devices that offer exceptional performance [115–118]. Since then, a lot of work has been done on the fabrication of 2D–2D heterostructures made by vertically and laterally stacking several 2D layered nanostructured types. These initiatives have made it possible to control and modify the generation, confinement, and transportation of charge carriers [119,120].

Beyond 2D–2D heterostructures, 2D–3D heterostructures, created by combining unique functionalities of 2D layered materials with standard 3D bulk materials, utilize both the benefits of 3D bulk materials as well as their innovative functions [121]. Although heterostructure and heterojunction are sometimes used interchangeably in the literature, a heterostructure device typically combines several heterojunctions. Normally, when two different materials are connected electrically, a heterojunction is formed at the boundary of the two materials. Charge transport via the interface causes a layer of depletion that results in band alignment because Fermi levels through the heterointerface tend to be balanced at a fixed energy level. The most important step in the heterostructure-based devices used for gas sensing is the adsorption and diffusion of analyte gas toward the heterojunction, which further changes junction properties and improves the sensor response by synergy effects [122,123].

6.8 THE APPEAL BEHIND METAL OXIDES-BASED HETEROSTRUCTURES

Compared to pure MOXs, sensors based on heterojunctions of MOXs show improved gas sensing performance toward the analyte gas. In contact with each other, the transfer of the carrier between the two materials is induced by the inconsistent Fermi levels at the interface. In n–n or n–p heterojunctions, the Fermi values of the two MOXs move to equilibrium, causing the energy bands to

bend and create potential barriers between them. The gas sensing performance of the investigated MOXs is mainly explained by redox reactions of the adsorption analyte gas on the surface of the sensor material. The changes in carrier concentration caused by the redox reaction on the composite surface may affect the height of the integrated potential barrier. This process has an additional effect on the resistance or conductivity of the sensor, which is based on n–n or n–p heterojunction as follows [124]:

$$\Delta R \propto \exp\left\{-\frac{\Delta eV_b}{K_B T}\right\} \tag{6.1}$$

where ΔR is the resistance change of the sensor, ΔV_b is the reduction of the height of the potential barrier, k_B is the Boltzmann constant, and T is the temperature [124,125]. As a result, small changes in the height of potential barriers would greatly affect the resistance of the sensor under study, which would improve the gas sensing properties of the heterojunction. In p–n or p–p heterostructures/heterojunctions, the interaction between the target gas and the sensing material also changes the sensor charge carrier, particularly holes, resulting in an additional variation in the thickness of the heterojunction accumulation layer and a more effective modulation of the carrier's conductor channel width. Therefore, sensors based on p–n or p–p heterojunction sensors also have improved the gas detection properties of reduced or oxidizing gases [117,126]. In addition, heterostructures consisting of heterojunctions of MOXs always have a specific surface higher than pure MOXs. The higher surface area allows the gas molecules to diffuse smoothly to the surface, interact more easily with the components, and provide more active sites. Using high specific surface areas increases the size of pores, facilitating the diffusion of gases into sensor materials, and increases the active surface of the internal component of the heterostructure for the adsorption of gases. Gas molecules' adsorption and desorption can also be accelerated in response and recovery processes based on the heterojunction of the MOXs. Thus, the high specific surface area is another positive factor that contributes to improved gas sensing performance in the heterostructure. Compared to the effects of specific surface areas, the study of enhanced gas detection mechanisms by heterojunctions of the MOX sensor materials is more complex. The role of heterojunctions in improving gas sensor performance should be analyzed in detail to fully understand their direct and significant effects on improving gas sensor performance. The gas sensor mechanism of MOX to common reducing and oxidizing gases was extensively discussed in the literature, and the effects of different often studied heterojunctions on improved gas sensor properties of composites were systematically investigated [123,126].

6.9 GAS SENSING PERFORMANCE OF 2D METAL OXIDE HETEROSTRUCTURES

Because it improves reaction and adsorption sites and results in higher catalytic activity than a single material, the development of heterostructures is a preferred method for improving gas sensing performance. When two different materials are combined, such as n–n, p–p, or n–p semiconductors, the interfaces have a synergistic effect that is equal to Fermi energy due to the electron transfer from the highest energy to the lowest energy level that is empty. Due to the band bending caused by different Fermi energies, a potential energy barrier is created in the contact. To overcome this potential energy barrier, electrons must cross the area of depletion (interface). The energy band diagram and heterojunctions manufactured with semiconductors n and p are shown in Figure 6.5. At the interface, an electron depletion layer with higher-energy conductivity band states is formed due to electron loss, as well as an electron accumulation layer with lower-energy conductivity band states [127]. Most of the charge carriers transferred from the higher to the lower state of the valence band at the p–p metal oxide heterojunction interface (Figure 6.5b) are holes containing the higher and lower states of the valence band. Due to its stability in low oxygen conditions and its compatibility with the measurement system, n-type materials are increasingly used [90]. A p–n heterojunction

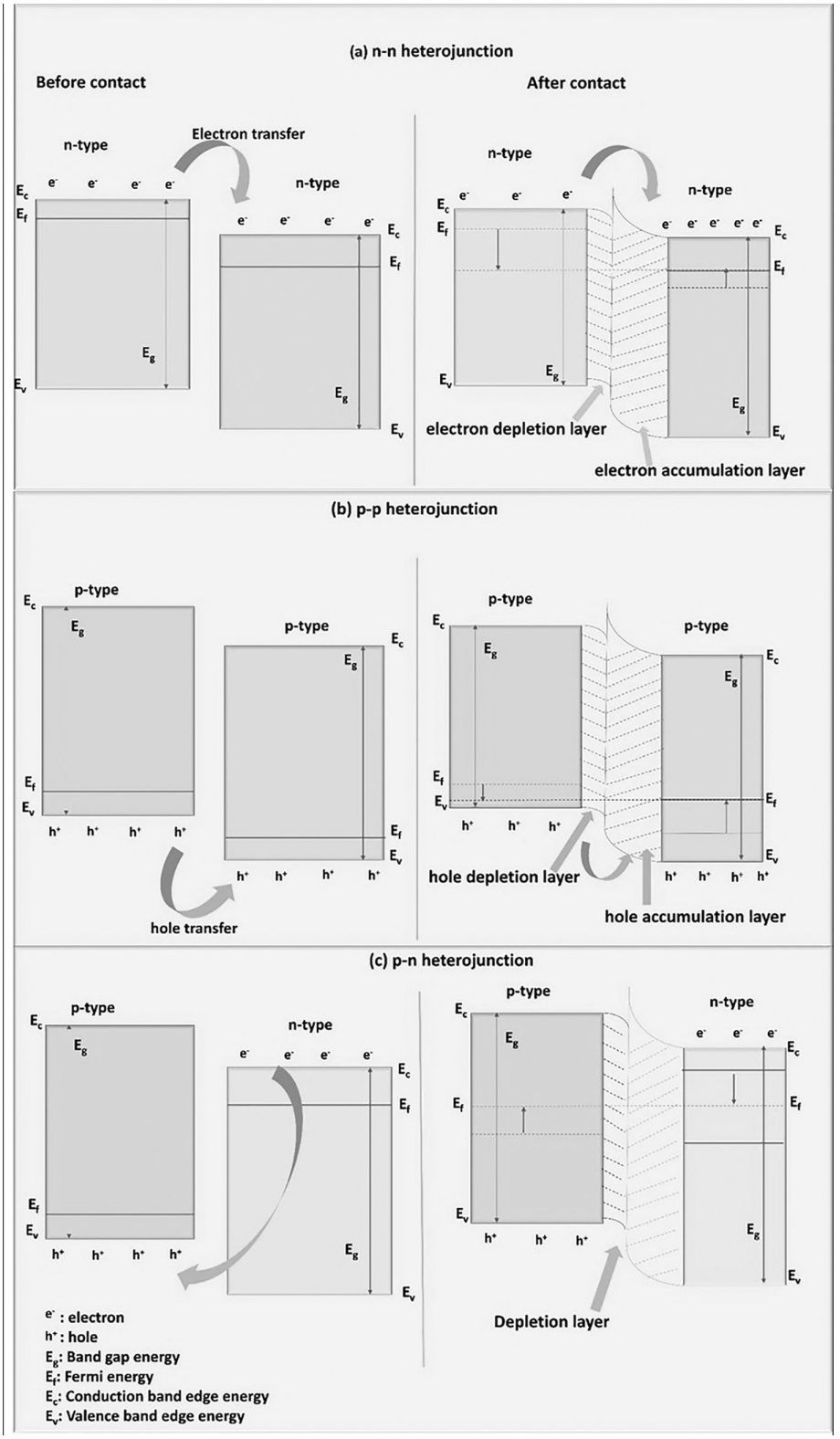

FIGURE 6.5 Types of heterojunctions build from (a) n–n, (b) p–p, and (c) p–n junctions.

can improve the performance of gas sensing. Depending on the backbone material, electron–hole recombination causes electron transfer from n-type to p-type or hole transfer from p-type to n-type at an n–p or p–n heterostructure interface (Figure 6.5c). This allows for more oxygen to be absorbed because of the higher electron density [122]. In comparison to n–n or p–p heterojunctions, these heterostructures have more free electrons [40,122]. There is a space charge area at the p–n interface because n-type materials often have intrinsic Fermi levels that are greater than p-type materials. Heterojunctions can accelerate electron transport and improve oxygen adsorption, resulting in an abundance of oxygen vacancies on the heterostructure surfaces and providing new active sites for higher sensing performances.

6.9.1 Heterojunction p–n Type Sensing Performance

A p–n heterojunction is created by combining a p-type semiconductor material with an n-type semiconductor material. This interface causes a bending of the energy bands and modifies the electronic properties at the junction. For example, Ju et al. [128] reported on the synthesis of ZnO/NiO heterostructures using a pulsed laser deposition technique, whereby they attached p-type NiO nanoparticles onto the surface of n-type ZnO nanosheets. When pure ZnO nanosheets are exposed to air at a high temperature, a depletion layer will form on the surface of the ZnO nanosheet due to the adsorption of oxygen molecules, leading to the high resistance state of sensing materials, as shown in Figure 6.6a and b. When NiO nanoparticles are embedded in the ZnO nanosheet surface, the electrons in ZnO and the holes in NiO diffuse in the opposite direction because of the great gradients of the same carrier concentration. Afterward, the internal electric field is generated in the interface of ZnO/NiO, and the spread of the carrier is finally balanced. After this, the energy band bends into the depletion layer until the system achieves a Fermi (E_F) level equilibrium (Figure 6.6e). Furthermore, the formation of the NiO/ZnO p–n interface with a new depletion layer at the interface increases the resistance of the sensor to further increase the air (Figure 6.6f). However, once the NiO/ZnO sensor is exposed to a reducing Triethylamine (TEA) gas, TEA reacts with oxygen ions absorbed on the surface of the ZnO nanosheet and releases electrons back to ZnO. Thus, the sensor resistance decreases. Furthermore, TEA releases electrons in NiO p-type and electron–hole recombination leads to a decrease in hole concentration. The decrease of holes in NiO results in the increase of electrons and reduces the concentration gradient. The reduction of holes in NiO increases electrons and reduces the concentration gradient of the same carrier on both sides of the p–n connection. As a result, the diffusion of the carriers is weakened, and the interface depletion layer becomes thin. Thus, the resistance of the NiO/ZnO sensor in TEA is even reduced. Figure 6.6g shows a model of the NiO/ZnO-based sensor when exposed to TEA gas. In comparison to the ZnO sensor, the formation of p–n junction in the NiO/ZnO-based sensor greatly increases air resistance and reduces TEA gas resistance. Therefore, based on the sensor response definition ($S = Ra/R_g$), the increase in S to TEA is mainly due to the resistance variation caused by the formation of p–n junction.

6.9.2 Heterojunctions p–p and n–n Types Sensing Performance

The creation of p–p and n–n heterojunctions provides band bending energy levels in an alike method as in p–n heterojunction. For p–n heterojunction, few electrons are involved at the interface due to electron–hole recombination that raises the resistance, whereas at the interface of n–n type heterojunction, there is just the transport of electrons from a material with higher Fermi level to lower Fermi level unoccupied state, making an accretion layer instead of a depletion layer. This accretion layer can be worn out by the successive oxygen adsorption on the surface, which certainly raises the potential energy barrier at the interface and enhances the sensing response.

In a study by Yang et al. [129], n–n type heterostructure based on CeO_2/SnO_2 was prepared and tested for 3H-2B sensing capabilities. Referring to Figure 6.7b, they reported that the Fermi

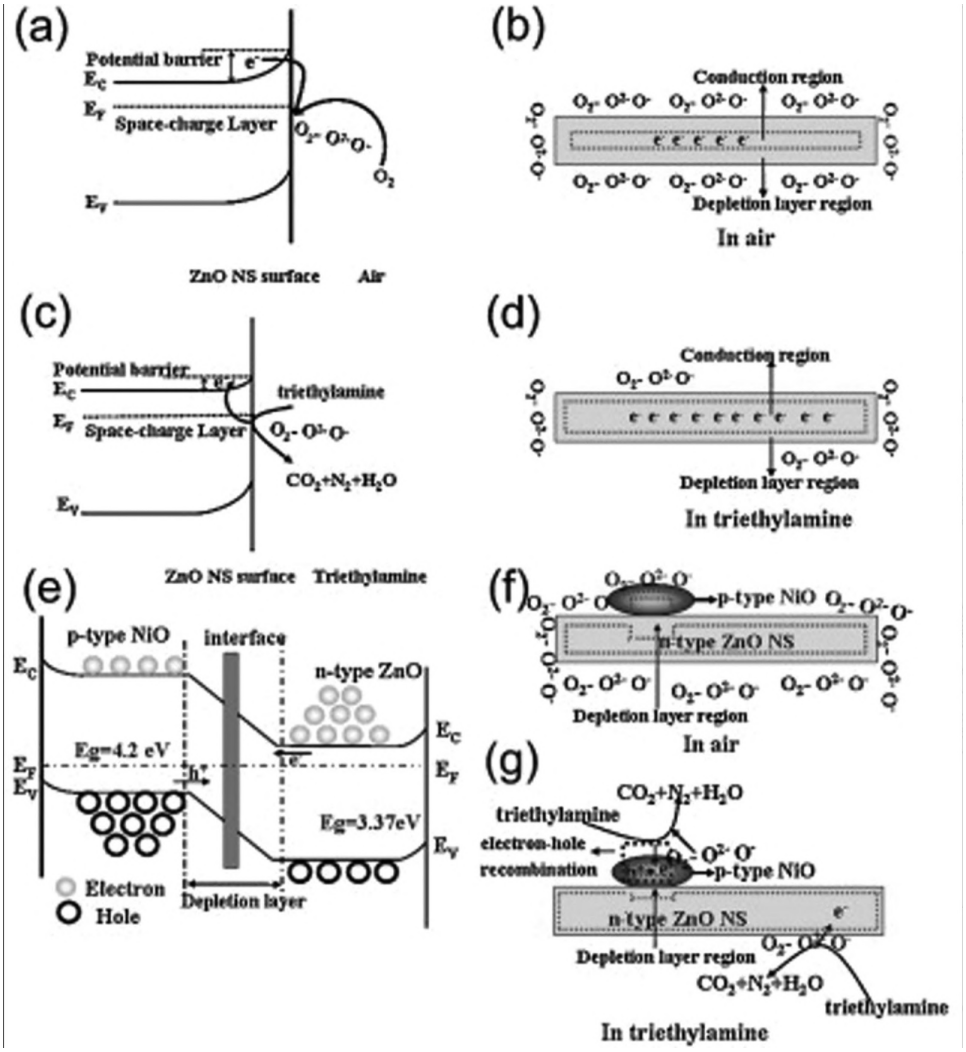

FIGURE 6.6 (a, b) The energy band diagram of ZnO nanosheet and its schematic model in air. (c, d) The energy band diagram of ZnO nanosheet and its schematic model in TEA. (e) The energy band diagram of p-type NiO and n-type ZnO heterostructure. (f, g) Schematic model for the ZNS sensor exposed to air and TEA gas, respectively. (Reproduced with permission from Ref. [128], Copyright © 2014 Elsevier.)

level of CeO_2 was higher than that of SnO_2, resulting in the electron transfer from CeO_2 to SnO_2 until achieving the equilibrium states of their Fermi levels. This would make an n–n type heterojunction at the interface and a depletion layer formed at the interface between CeO_2 and SnO_2 and increase the potential barrier height built into the air due to oxygen adsorption. Normally, the oxygen molecules prefer to be adsorbed on the asymmetric Ce-O-Sn sites to predominantly dissociate to active O^-(ads) species on the surface of the porous CeO_2/SnO_2 nanosheets. When 3H-2B gas is introduced, it interacts with the adsorbed oxygen species on the surfaces, and electrons are released back to the conduction band of CeO_2/SnO_2 nanosheets. The released electrons would decrease the thickness of the depletion layers between CeO_2 and SnO_2, further resulting in a decrease in the height of the potential barrier. This process would increase the conductivity of the sensor and significantly enhance the 3H-2B sensing performance of the CeO_2/SnO_2 nanosheets. Coupled with results from DFT, they showed that the active O^-(ad) species originated from the

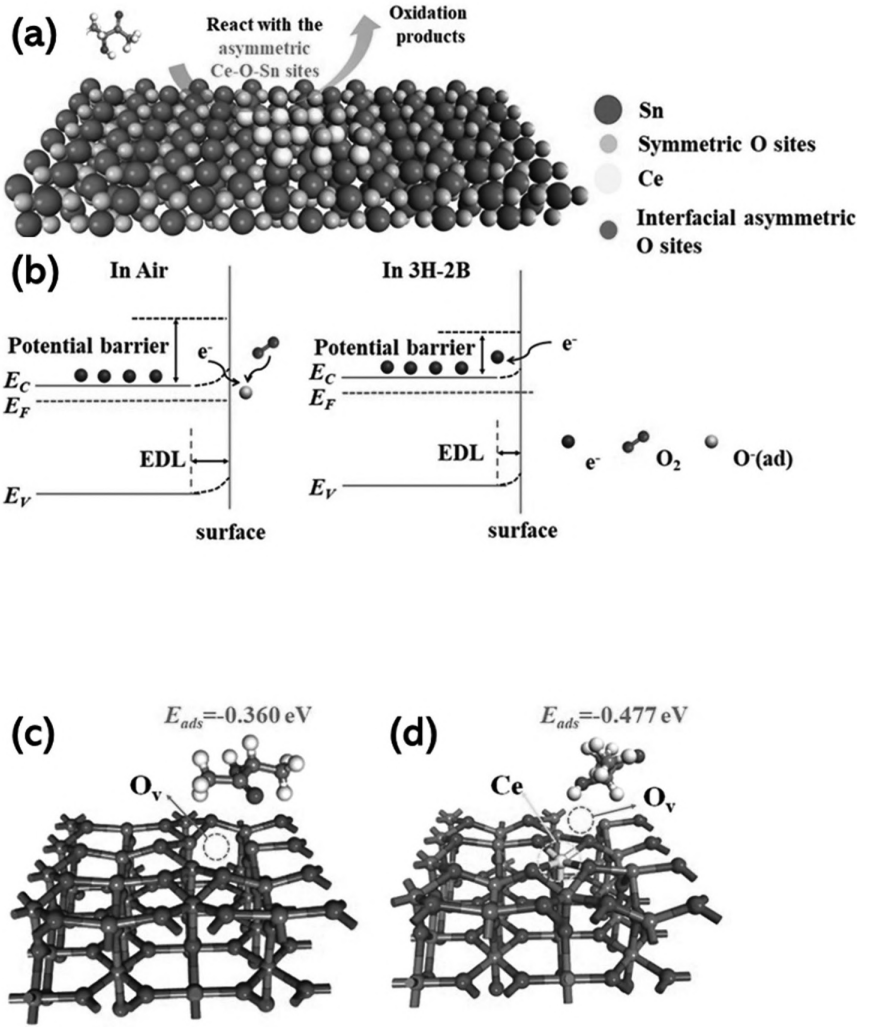

FIGURE 6.7 (a) Demonstration of the surface sensing mechanism of 3H-2B on CeO_2/SnO_2 nanosheets surface, (b) demonstrations of the 3H-2B sensing mechanism band diagrams for CeO_2/SnO_2-400 nanosheets, (c) adsorption configurations of 3H-2B adsorbed on O_v of SnO_2, and (d) O_v near asymmetric Ce-O-Sn sites of CeO_2-SnO_2 interface. (Reproduced with permission from Ref. [129], Copyright © 2022 Elsevier.)

asymmetric Ce-O-Sn sites, as the adsorption energy (E_{ads}) for 3H-2B on (110) plane of SnO_2 was calculated to be −0.477 eV for asymmetric Ce-O-Sn sites and that of symmetric Sn-O-Sn sites was −0.36 eV, as depicted in Figure 6.7c and d, which further enhanced the adsorption and reaction kinetics of 3H-2B on the CeO_2/SnO_2 nanosheets surface, thus resulting in quicker response and recovery times. The porous 2D MOX nanosheet structure in this case endowed the materials with more surface-active sites and a much shorter diffusion pathway, which is highly desirable for the diffusion and adsorption of 3H-2B molecules on the surface of the material, further improving their sensing performance. It was also demonstrated that the local environment of oxygen species influences the sensing performance.

Porous MoO_3/SnO_2 nanoflakes with n–n junctions were also reported by Gao et al. [130] to demonstrate an improved gas sensing property with a higher gas sensor response of 43.5 toward 10 ppm H_2S at 115°C compared with that of the pure SnO_2. The improved H_2S sensing performance was attributed to the formation of n–n junctions, which played an important role in enhancing the

sensing characteristics of MoO_3/SnO_2 nanoflakes. Also, the BET surface area of the heterostructure was found to be around 1.8 times larger than that of the pure SnO_2 nanoflakes. Because of this, more gas molecules were able to participate in surface reactions leading to a greater change in the resistance when the heterostructure was exposed to different gas atmospheres. Additionally, the heterostructure nanoflakes possessed larger pore volume than that of the pure SnO_2 nanoflakes and larger pore volume advances gas diffusion, facilitating the enhancement of H_2S sensing performance [130]. Other remarkable achievements in the use of n–n type MOXs for chemical gas sensing have been reported including WO_3@SnO_2 core–shell nanosheets [131], SnO_2:CeO_2 nanosheets [132], and TiO_2/SnO_2 nanosheets [133]. Their sensor performance has been summarized in Table 6.1.

In the p–p type heterojunction, the gas sensing is similar, but the dominant charge carriers are holes and the change in resistance after interaction with analyte gases is reversed in comparison to the n–n type heterojunction. For example, after the heterojunction of NiO-CuO [134] forms at the interface between NiO and CuO (Figure 6.8), a hole depletion layer and a hole accumulation layer form at the interfaces of NiO and CuO. The adsorbed oxygen ions create holes in the hole depletion layer, making them thinner than pure NiO and less resistant. The reaction between H_2S molecules and deposited oxygen ions fills holes and increases the resistance measured when the heterojunction is exposed to H_2S.

Table 6.1 summarizes some of the works found in the literature on 2D MOXs and their heterostructures-based sensing materials. The gas sensing performance including the operating temperature, response, analyte gas and concentration, response, and recovery rate has been summarized. A lot of progress has been made in the chemical gas sensor space, particularly in the use of MOX-based materials, and as evidenced by the referenced works.

6.10 CONCLUSION AND FUTURE OUTLOOK

Over the past two decades, research into 2D MOX materials has been ongoing, and all literature works have paved the way, leaving no doubt about the potential of 2D MOX materials for sensing applications. The research in the sensor technology space is based on a long-term goal of commercializing sensing devices that contain 2D MOX materials. The key industrial aspects to get these devices commercialized are to find 2D MOX development techniques that are reliable and are of low-cost production and scalable. 2D MOX materials are made up of traditional MOXs such as ZnO, TiO_2, and NiO, and the perovskite oxide family and LDHs do have a potential for industrial production based on their characteristics that are beneficial for gas sensing. However, traditional MOXs suffer from high operating temperatures, making them highly energy-consuming. Even though LDHs have unique physicochemical properties such as high surface area and high porosity, anion and cation exchange capacity, and adjustable structure engineering with high controllability, they have drawbacks including agglomeration and low conductivity, which make their use in gas sensing to be limited.

Progress in the manufacturing process of 2D MOX materials has enabled the pairing of 2D structures with different dimensions to form heterostructures. The idea of combining various MOX materials to form heterostructures is relatively recent and stems from the need to improve the selectiveness and other important sensor parameters of chemical gas sensors, such as operating temperature, selectivity, and stability. Heterostructure materials present strong interactions between closely packed interfaces, giving superior performance compared to the construction of single MOX materials. It has also been widely reported that smaller molecules exhibit higher reactions in microstructures of similar sizes, thereby demonstrating higher selectivity. Since wide-band-gap materials generally have fewer reactions, heterostructure materials can be selected to increase surface reactivity through surface–gas interactions. 2D MOX heterostructures-based materials have shown higher possibilities of being used for developing high-performance sensors for detection of different analytical gases. Nonetheless, many discoveries and detailed research remain to be made to fully recognize the opportunities of these materials to realize commercialization. The utilization of DFT

TABLE 6.1
Performance of Gas Sensors Based on 2D Metal Oxides Nanostructures and Their Heterostructures

2D Metal Oxide	Method	Gas	Temp. (°C)	Response	T_{res}/Rec (s)	Ref.
ZnO nanosheets	Hydrothermal	Acetylacetone, 100 ppm	340	191.1	19/94	[73]
ZnO nanosheets	Solvothermal	NO_2, 10 ppm	200	74.68	–	[135]
In_2O_3 nanosheets	Hydrothermal	NO_X, 10 ppm	120	213	4/10	[136]
SnO_2 nanosheets	Hydrothermal	HCHO	240	3	–	[31]
MoO_3 nanosheets	Exfoliation	C_2H_6O	300	33	21/10	[137]
MoO_3, nanosheets	Hydrothermal	DIPA, 10 ppm	217	30.4	4.3/–	[138]
WO_3 nanosheets	Chemical bath deposition	NO_2, 10 ppm	100	460	54/63	[139]
NiO nanosheets	Hydrothermal	NO_2, 20 ppm	250	80%	–	[140]
NiO lotus-root slice-shaped	Hydrothermal	N_2H_4, 100 ppm	92	107.6	50/29.6	[141]
Co_3O_4 nanosheets	Hydrothermal	Acetone, 100 ppm	150	11.4	150-41/300-65	[142]
Co_3O_4	Solvothermal	Xylene, 100 ppm	150	74.5	–	[143]
$NbWO_6$ Perovskite	High-temperature calcination	H_2S, 50 ppm	150	12.5	6/30	[37]
$LaCoO_3$ - ZnO	Sol–gel method	Ethanol,100 ppm	320	55	2.8/9.7	[144]
LDH- Ag/LDH	Glucose reduction	Methanol, 100 ppm	RT	3.35	10/20	[145]
Pd/TiO_2 nanosheets	GO template	H_2, 1000 ppm	230	9.1	1.6/1.4	[146]
WO_3-rGO nanoflakes	Hydrothermal	NO_2, 10 ppm	90	4	10/9	[147]
TiO_2/SnO_2 nanosheets	PLD	TEA, 100 ppm	260	52.3	12/22	[133]
SnO_2:CeO_2 nanosheets	Hydrothermal	Ethanol, 100 ppm	340	44	25/6	[132]
NiO/Co_3O_4 nanosheets	Hydrothermal	Xylene, 100 ppm	140	12.27	22/55	[148]
ZnO-SnO_2 nanosheets	Co-precipitation and decomposition	Ethanol, 50 ppm	240	80	7/42	[149]
CeO_2/ZnO nanosheets	Hydrothermal	Ethanol, 100 ppm	310	90	20/4	[150]
Co_3O_4/MoS_2 nanosheets	In-situ anchored	NH_3, 5 ppm	RT	2.1	105/355	[151]
Pt-$BiVO_4$ nanosheets	Colloidal	Acetone, 100 pm	300	12.5	–	[152]

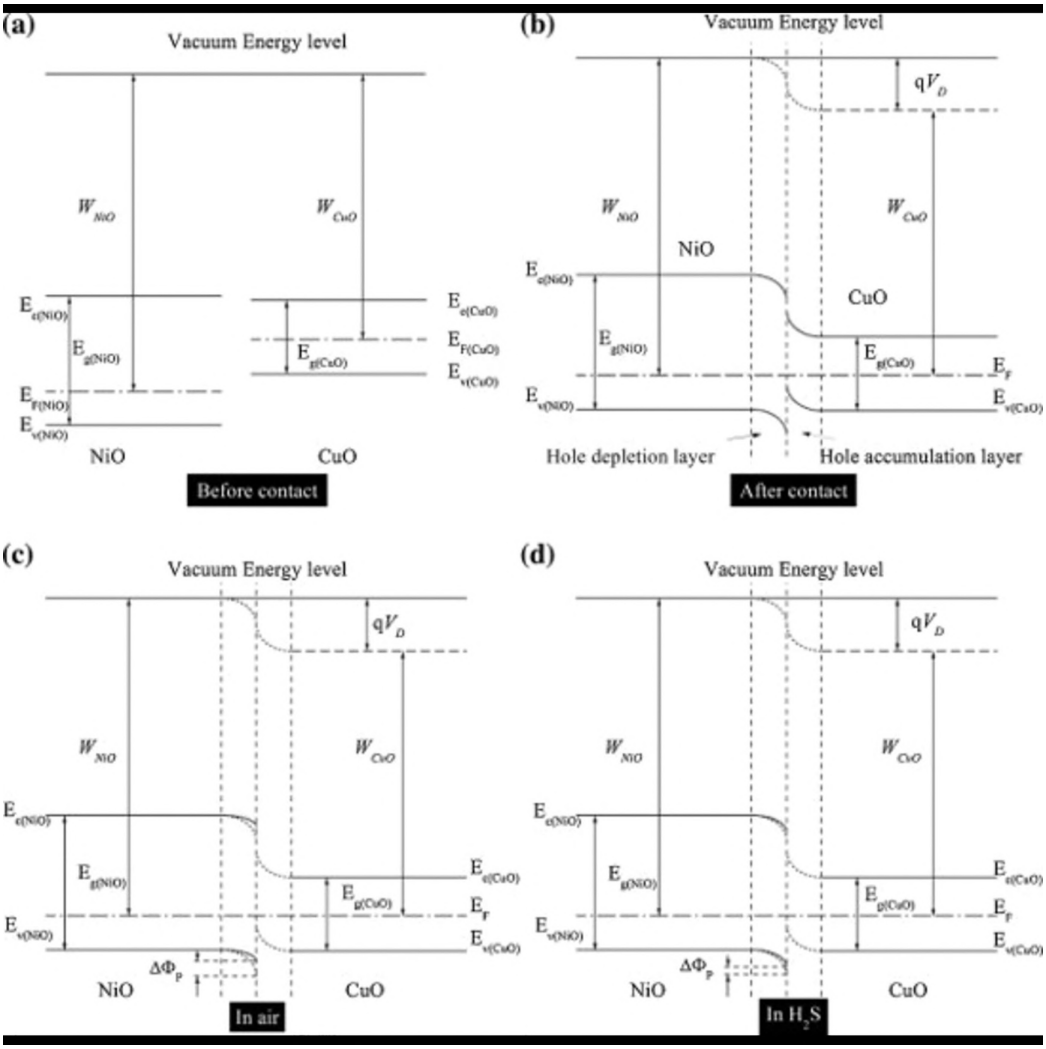

FIGURE 6.8 Schematic diagrams of the energy band structure of NiO and CuO (a) before and (b) after contact. CuO-NiO heterostructures (c) in air and (d) in H_2S. (Reproduced with permission from Ref. [134], Copyright © 2015 Elsevier.)

studies will significantly contribute to the rapid and comprehensive advancement of 2D MOX materials in the field of gas sensing. This is primarily attributed to DFT's capability to offer a profound understanding of atomic geometries and the underlying chemical bonding, thereby serving as a valuable tool for understanding surface–adsorbate interactions through the precise determination of their adoption energy and electronic properties.

ACKNOWLEDGMENTS

The authors would like to acknowledge the Department of Science and Innovation (DSI), MINTEK Advanced Materials Division (AMD), Council for Scientific and Industrial Research (CSIR), and University of Venda, South Africa for financial support.

REFERENCES

1. Kgomo, M.B., Shingange, K., Nemufulwi, M.I., Swart, H.C., Mhlongo, G.H. Belt-like In_2O_3 based sensor for methane detection: Influence of morphological, surface defects and textural behavior. *Materials Research Bulletin*. 158 (2023) 112076. https://doi.org/10.1016/j.materresbull.2022.112076.
2. Nemufulwi, M.I., Swart, H.C., Shingange, K., Mhlongo, G.H. ZnO/$ZnFe_2O_4$ heterostructure for conductometric acetone gas sensors. *Sensors and Actuators B: Chemical*. 377 (2023) 133027. https://doi.org/10.1016/j.snb.2022.133027.
3. Shingange, K., Swart, H.C., Mhlongo, G.H. Enhanced ethanol sensing abilities of fiber-like $La_{1-x}Ce_x$-CoO3($0 \leq x \leq 0.2$) perovskites based-sensors at low operating temperatures. *Sensors and Actuators B: Chemical*. 377 (2023) 133012. https://doi.org/10.1016/j.snb.2022.133012.
4. Talwar, V., Singh, O., Singh, R.C. ZnO assisted polyaniline nanofibers and its application as ammonia gas sensor. *Sensors and Actuators B: Chemical*. 191 (2014) 276–282. https://doi.org/10.1016/j.snb.2013.09.106.
5. Thepnurat, M., Chairuangsri, T., Hongsith, N., Ruankham, P., Choopun, S. Realization of interlinked ZnO tetrapod networks for UV sensor and room-temperature gas sensor. *ACS Applied Materials & Interfaces*. 7 (2015) 24177–24184. https://doi.org/10.1021/acsami.5b07491.
6. Meng, Z., Stolz, R.M., Mendecki, L., Mirica, K.A. Electrically-transduced chemical sensors based on two-dimensional nanomaterials. *Chemical Reviews*. 119 (2019) 478–598. https://doi.org/10.1021/acs.chemrev.8b00311.
7. Minh Triet, N., Thai Duy, L., Hwang, B., Hanif, A., Siddiqui, S., Park, K., Cho, C., Lee, N. High-Performance schottky diode gas sensor based on the heterojunction of three-dimensional nanohybrids of reduced graphene oxide–vertical ZnO nanorods on an AlGaN/GaN layer. *ACS Applied Materials & Interfaces*. 9 (2017) 30722–30732. https://doi.org/10.1021/acsami.7b06461.
8. Lazanas, A.C., Prodromidis, M.I. Two-dimensional inorganic nanosheets: production and utility in the development of novel electrochemical (bio)sensors and gas-sensing applications. *Microchimica Acta*. 188 (2021) 1–34. https://doi.org/10.1007/s00604-020-04674-0.
9. Paul, A., Muthukumar, S., Prasad, S. Review—room-temperature ionic liquids for electrochemical application with special focus on gas sensors. *Journal of the Electrochemical Society*. 167 (2019) 037511. https://doi.org/10.1149/2.0112003JES.
10. Shin, W., Goto, T., Nagai, D., Itoh, T., Tsuruta, A., Akamatsu, T., Sato, K. Thermoelectric array sensors with selective combustion catalysts for breath gas monitoring. *Sensors*. 18 (2018) 1579. https://doi.org/10.3390/s18051579.
11. Yu, Y., Hu, Z., Lien, S., Yu, Y., Gao, P. Self-powered thermoelectric hydrogen sensors based on low-cost bismuth sulfide thin films: Quick response at room temperature. *ACS Applied Materials & Interfaces*. 14 (2022) 47696–47705. https://doi.org/10.1021/acsami.2c12749.
12. Kirchner, P., Oberländer, J., Suso, H., Rysstad, G., Keusgen, M., Schöning, M.J. Monitoring the microbicidal effectiveness of gaseous hydrogen peroxide in sterilisation processes by means of a calorimetric gas sensor. *Food Control*. 31 (2013) 530–538. https://doi.org/10.1016/j.foodcont.2012.11.048.
13. Yun, J., Cho, M., Lee, K., Kang, M., Park, I. A review of nanostructure-based gas sensors in a power consumption perspective. *Sensors and Actuators B: Chemical*. 372 (2022) 132612. https://doi.org/10.1016/j.snb.2022.132612.
14. Paliwal, A., Sharma, A., Tomar, M., Gupta, V. Carbon monoxide (CO) optical gas sensor based on ZnO thin films. *Sensors and Actuators B: Chemical*. 250 (2017) 679–685. https://doi.org/10.1016/j.snb.2017.05.064.
15. Kang, X., Yip, S., Meng, Y., Wang, W., Li, D., Liu, C., Ho, J.C. High-performance electrically transduced hazardous gas sensors based on low-dimensional nanomaterials. *Nanoscale Advances*. 3 (2021) 6254–6270. https://doi.org/https://doi.org/10.1039/D1NA00433F.
16. Dey, A. Semiconductor metal oxide gas sensors: A review. *Materials Science and Engineering B*. 229 (2018) 206–217. https://doi.org/10.1016/j.mseb.2017.12.036.
17. Wang, C., Yin, L., Zhang, L., Xiang, D., Gao, R. Metal oxide gas sensors: sensitivity and influencing factors. *Sensors*. 10 (2010) 2106. https://doi.org/10.3390/s100302088.
18. Bannov, A.G., Popov, M.V., Brester, A.E., Kurmashov, P.B. Recent advances in ammonia gas sensors based on carbon nanomaterials. *Micromachines*. 12 (2021) 186. https://doi.org/https://doi.org/10.3390/mi12020186.
19. Kumar, V., Raghuwanshi, S.K., Kumar, S. Recent advances in carbon nanomaterials based SPR sensor for biomolecules and gas detection—A review. *IEEE Sensors Journal*. 22 (2022) 15661–15672. https://doi.org/10.1109/JSEN.2022.3191042.

20. Llobet, E. Gas sensors using carbon nanomaterials: A review. *Sensors and Actuators B: Chemical*. 179 (2013) 32–45. https://doi.org/10.1016/j.snb.2012.11.014.
21. Liu, X., Zheng, W., Kumar, R., Kumar, M., Zhang, J. Conducting polymer-based nanostructures for gas sensors. *Coordination Chemistry Reviews*. 462 (2022) 214517. https://doi.org/10.1016/j.ccr.2022.214517.
22. Pavel, I., Lakard, S., Lakard, B. Flexible sensors based on conductive polymers. *Chemosensors*. 10 (2022) 97. https://doi.org/10.3390/chemosensors10030097.
23. Nikolic, M.V., Milovanovic, V., Vasiljevic, Z.Z., Stamenkovic, Z. Semiconductor gas sensors: Materials, technology, design, and application. *Sensors*. 20 (2020) 6694. https://doi.org/10.3390/s20226694.
24. Lee, S., Galstyan, V., Ponzoni, A., Gonzalo-Juan, I., Riedel, R., Dourges, M., Nicolas, Y., Toupance, T. Finely tuned SnO_2 nanoparticles for efficient detection of reducing and oxidizing gases: The influence of alkali metal cation on gas-sensing properties. *ACS Applied Materials Interfaces*. 10 (2018) 10173–10184. https://doi.org/10.1021/acsami.7b18140.
25. Liang, Y., Yang, Y., Zou, C., Xu, K., Luo, X., Luo, T., Li, J., Yang, Q., Shi, P., Yuan, C. 2D ultra-thin WO_3 nanosheets with dominant {002} crystal facets for high-performance xylene sensing and methyl orange photocatalytic degradation. *Journal of Alloys and Compounds*. 783 (2019) 848–854. https://doi.org/10.1016/j.jallcom.2018.12.384.
26. Wang, T.T., Ma, S.Y., Cheng, L., Xu, X.L., Luo, J., Jiang, X.H., Li, W.Q., Jin, W.X., Sun, X.X. Performance of 3D SnO_2 microstructure with porous nanosheets for acetic acid sensing. *Materials Letters*. 142 (2015) 141–144. https://doi.org/10.1016/j.matlet.2014.12.009.
27. Xiao, Y., Lu, L., Zhang, A., Zhang, Y., Sun, L., Huo, L., Li, F. Highly enhanced acetone sensing performances of porous and single crystalline ZnO nanosheets: High percentage of exposed (100) facets working together with surface modification with Pd nanoparticles. *ACS Applied Materials & Interfaces*. 4 (2012) 3797–3804. https://doi.org/10.1021/am3010303.
28. Zhao, C., Gong, H., Lan, W., Ramachandran, R., Xu, H., Liu, S., Wang, F. Facile synthesis of SnO_2 hierarchical porous nanosheets from graphene oxide sacrificial scaffolds for high-performance gas sensors. *Sensors and Actuators B: Chemical*. 258 (2018) 492–500. https://doi.org/10.1016/j.snb.2017.11.167.
29. Liu, X., Sun, Y., Yu, M., Yin, Y., Du, B., Tang, W., Jiang, T., Yang, B., Cao, W., Ashfold, M.N.R. Enhanced ethanol sensing properties of ultrathin ZnO nanosheets decorated with CuO nanoparticles. *Sensors and Actuators B: Chemical*. 255 (2018) 3384–3390. https://doi.org/10.1016/j.snb.2017.09.165.
30. Shinde, R.B., Padalkar, N.S., Sadavar, S.V., Kale, S.B., Magdum, V.V., Chitare, Y.M., Kulkarni, S.P., Patil, U.M., Parale, V.G., Park, H., Gunjakar, J.L. 2D–2D lattice engineering route for intimately coupled nanohybrids of layered double hydroxide and potassium hexaniobate: Chemiresistive SO_2 sensor. *Journal of Hazardous Materials*. 432 (2022) 128734. https://doi.org/10.1016/j.jhazmat.2022.128734.
31. Yu, H., Yang, T., Zhao, R., Xiao, B., Li, Z., Zhang, M. Fast formaldehyde gas sensing response properties of ultrathin SnO_2 nanosheets. *RSC Advances*. 5 (2015) 104574–104581. https://doi.org/10.1039/C5RA22755K.
32. Apte, A., Mozaffari, K., Samghabadi, F.S., Hachtel, J.A., Chang, L., Susarla, S., Idrobo, J.C., Moore, D.C., Glavin, N.R., Litvinov, D. 2D electrets of ultrathin MoO_2 with apparent piezoelectricity. *Advvanced Materials*. 32 (2020) 2000006. https://doi.org/https://doi.org/10.1002/adma.202000006.
33. Haque, F., Daeneke, T., Kalantar-zadeh, K., Ou, J.Z. Two-dimensional transition metal oxide and chalcogenide-based photocatalysts. *Nano-Micro Letters*. 10 (2017) 23. https://doi.org/10.1007/s40820-017-0176-y.
34. Zhang, B.Y., Xu, K., Yao, Q., Jannat, A., Ren, G., Field, M.R., Wen, X., Zhou, C., Zavabeti, A., Ou, J.Z. Hexagonal metal oxide monolayers derived from the metal–gas interface. *Nature Materials*. 20 (2021) 1073–1078. https://doi.org/10.1038/s41563-020-00899-9.
35. Xie, H., Li, Z., Cheng, L., Haidry, A.A., Tao, J., Xu, Y., Xu, K., Ou, J.Z. Recent advances in the fabrication of 2D metal oxides. *iScience*. 25 (2022) 1–30. https://doi.org/10.1016/j.isci.2021.103598
36. Addabbo, T., Bertocci, F., Fort, A., Gregorkiewitz, M., Mugnaini, M., Spinicci, R., Vignoli, V. Gas sensing properties and modeling of $YCoO_3$ based perovskite materials. *Sensors Actuators B: Chemical*. 221 (2015) 1137–1155. https://doi.org/https://doi.org/10.1016/j.snb.2015.07.079.
37. Wang, J., Ren, Y., Liu, H., Li, Z., Liu, X., Deng, Y., Fang, X. Ultrathin 2D $NbWO_6$ perovskite semiconductor based gas sensors with ultrahigh selectivity under low working temperature. *Advanced Materials*. 34 (2022) 2104958. https://doi.org/10.1002/adma.202104958.
38. Sowmya, B., John, A., Panda, P.K. A review on metal-oxide based pn and nn heterostructured nanomaterials for gas sensing applications. *Sensors International*. 2 (2021) 100085. https://doi.org/https://doi.org/10.1016/j.sintl.2021.100085.
39. Guo, W., Fu, M., Zhai, C., Wang, Z. Hydrothermal synthesis and gas-sensing properties of ultrathin hexagonal ZnO nanosheets. *Ceramics International*. 40 (2014) 2295–2298. https://doi.org/10.1016/j.ceramint.2013.07.150.

40. Miller, D.R., Akbar, S.A., Morris, P.A. Nanoscale metal oxide-based heterojunctions for gas sensing: A review. *Sensors and Actuators B: Chemical*. 204 (2014) 250–272. https://doi.org/10.1016/j.snb.2014.07.074.
41. Tshabalala, Z.P., Shingange, K., Cummings, F.R., Ntwaeaborwa, O.M., Mhlongo, G.H., Motaung, D.E. Ultra-sensitive and selective NH_3 room temperature gas sensing induced by manganese-doped titanium dioxide nanoparticles. *Journal of Colloid and Interface Science*. 504 (2017) 371–386. https://doi.org/10.1016/j.jcis.2017.05.061.
42. Zakaria, S.A., Ahmadi, S.H., Amini, M.H. Chemiresistive gas sensors based on layered double hydroxides (LDHs) structures: A review. *Sensors and Actuators A: Physical*. 346 (2022) 113827. https://doi.org/10.1016/j.sna.2022.113827.
43. Moseley, P.T. Progress in the development of semiconducting metal oxide gas sensors: A review. *Measurement Science and Technology*. 28 (2017) 082001. https://doi.org/10.1088/1361-6501/aa7443.
44. Wetchakun, K., Samerjai, T., Tamaekong, N., Liewhiran, C., Siriwong, C., Kruefu, V., Wisitsoraat, A., Tuantranont, A., Phanichphant, S. Semiconducting metal oxides as sensors for environmentally hazardous gases. *Sensors and Actuators B: Chemical*. 160 (2011) 580–591. https://doi.org/10.1016/j.snb.2011.08.032.
45. Yu, K., Lei, D., Feng, Y., Yu, H., Chang, Y., Wang, Y., Liu, Y., Wang, G., Lou, L., Liu, S., Zhou, W. The role of Bi-doping in promoting electron transfer and catalytic performance of Pt/3DOM-$Ce_{1-x}Bi_xO_{2-\delta}$. *Journal of Catalysis*. 365 (2018) 292–302. https://doi.org/10.1016/j.jcat.2018.06.025.
46. Yang, C.S., Shang, D.S., Liu, N., Shi, G., Shen, X., Yu, R.C., Li, Y.Q., Sun, Y. A synaptic transistor based on quasi-2D molybdenum oxide. *Advanced Materials*. 29 (2017) 1700906. https://doi.org/10.1002/adma.201700906.
47. Momma, K., Izumi, F. VESTA 3 for three-dimensional visualization of crystal, volumetric and morphology data. *Journal of Applied Crystallography*. 44 (2011) 1272–1276. https://doi.org/https://doi.org/10.1107/S0021889811038970.
48. Wang, Y., Ren, B., Zhen Ou, J., Xu, K., Yang, C., Li, Y., Zhang, H. Engineering two-dimensional metal oxides and chalcogenides for enhanced electro- and photocatalysis. *Science Bulletin*. 66 (2021) 1228–1252. https://doi.org/10.1016/j.scib.2021.02.007.
49. Wang, Q., O'Hare, D. Recent advances in the synthesis and application of layered double hydroxide (LDH) nanosheets. *Chemical Reviews*. 112 (2012) 4124–4155. https://doi.org/10.1021/cr200434v.
50. Fahami, A., Al-Hazmi, F.S., Al-Ghamdi, A.A., Mahmoud, W.E., Beall, G.W. Structural characterization of chlorine intercalated Mg-Al layered double hydroxides: A comparative study between mechanochemistry and hydrothermal methods. *Journal of Alloys and Compounds*. 683 (2016) 100–107. https://doi.org/10.1016/j.jallcom.2016.05.032.
51. Khan, A.I., O'Hare, D. Intercalation chemistry of layered double hydroxides: recent developments and applications. *Journal of Materials Chemistry*. 12 (2002) 3191–3198. https://doi.org/10.1039/B204076J.
52. Theiss, F.L., Couperthwaite, S.J., Ayoko, G.A., Frost, R.L. A review of the removal of anions and oxyanions of the halogen elements from aqueous solution by layered double hydroxides. *Journal of Colloid and Interface Science*. 417 (2014) 356–368. https://doi.org/10.1016/j.jcis.2013.11.040.
53. Polese, D., Mattoccia, A., Giorgi, F., Pazzini, L., Di Giamberardino, L., Fortunato, G., Medaglia, P.G. A phenomenological investigation on Chlorine intercalated Layered Double Hydroxides used as room temperature gas sensors. *Journal of Alloys and Compounds*. 692 (2017) 915–922. https://doi.org/10.1016/j.jallcom.2016.09.125.
54. Ru, L., Li, Z., Bai, C., Zhang, N., Wang, H. Effect of $CaTiO_3$ crystal structure and cathodic morphological structure on the electrolysis. *Asian Journal of Chemistry*. 25 (2013) 1814. https://doi.org/10.14233/ajchem.2013.13162.
55. Danaie, M., Kepaptsoglou, D., Ramasse, Q.M., Ophus, C., Whittle, K.R., Lawson, S.M., Pedrazzini, S., Young, N.P., Bagot, P.A.J., Edmondson, P.D. Characterization of ordering in A-site deficient perovskite $Ca_{1-x}La_{2x/3}TiO_3$ using STEM/EELS. *Inorganic Chemistry*. 55 (2016) 9937–9948. https://doi.org/10.1021/acs.inorgchem.6b02087.
56. Kumbhakar, P., Chowde Gowda, C., Mahapatra, P.L., Mukherjee, M., Malviya, K.D., Chaker, M., Chandra, A., Lahiri, B., Ajayan, P.M., Jariwala, D., Singh, A., Tiwary, C.S. Emerging 2D metal oxides and their applications. *Materials Today*. 45 (2021) 142–168. https://doi.org/10.1016/j.mattod.2020.11.023.
57. Raza, A., Zhang, Y., Cassinese, A., Li, G. Engineered 2D metal oxides for photocatalysis as environmental remediation: A theoretical perspective. *Catalysts*. 12 (2022) 1613. https://doi.org/10.3390/catal12121613.
58. Dral, A.P., ten Elshof, J.E. 2D metal oxide nanoflakes for sensing applications: Review and perspective. *Sensors Actuators B: Chemical*. 272 (2018) 369–392. https://doi.org/10.1016/j.snb.2018.05.157.
59. Fine, G.F., Cavanagh, L.M., Afonja, A., Binions, R. Metal oxide semi-conductor gas sensors in environmental monitoring. *Sensors*. 10 (2010) 5502. https://doi.org/10.3390/s100605469.

60. Lin, T., Lv, X., Li, S., Wang, Q. The morphologies of the semiconductor oxides and their gas-sensing properties. *Sensors*. 17 (2017) 2779. https://doi.org/10.3390/s17122779.
61. Singh, E., Meyyappan, M., Nalwa, H.S. Flexible graphene-based wearable gas and chemical sensors. *ACS Applied Materials & Interfaces*. 9 (2017) 34544–34586. https://doi.org/10.1021/acsami.7b07063.
62. Yoon, Y., Truong, P.L., Lee, D., Ko, S.H. Metal-oxide nanomaterials synthesis and applications in flexible and wearable sensors. *ACS Nanoscience Au*. 2 (2022) 64–92. https://doi.org/10.1021/acsnanoscienceau.1c00029.
63. Kanaparthi, S., Govind Singh, S. Highly sensitive and ultra-fast responsive ammonia gas sensor based on 2D ZnO nanoflakes. *Materials Science for Energy Technologies*. 3 (2020) 91–96. https://doi.org/10.1016/j.mset.2019.10.010.
64. Shendage, S.S., Patil, V.L., Vanalakar, S.A., Patil, S.P., Harale, N.S., Bhosale, J.L., Kim, J.H., Patil, P.S. Sensitive and selective NO_2 gas sensor based on WO_3 nanoplates. *Sensors and Actuators B: Chemical*. 240 (2017) 426–433. https://doi.org/10.1016/j.snb.2016.08.177.
65. Timmerman, M.A., Xia, R., Le, P.T., Wang, Y., Ten Elshof, J.E. Metal oxide nanosheets as 2D building blocks for the design of novel materials. *Chemistry–A European Journal*. 26 (2020) 9084–9098. https://doi.org/10.1002/chem.201905735.
66. Neri, G. Thin 2D: The new dimensionality in gas sensing. *Chemosensors*. 5 (2017) 21. https://doi.org/10.3390/chemosensors5030021.
67. Dima, R.S., Tshwane, D.M., Shingange, K., Modiba, R., Maluta, N.E., Maphanga, R.R. Adsorption of NH_3 and NO_2 molecules on Sn-doped and undoped ZnO (101) surfaces using density functional theory. *Processes*. 10 (2022) 2027. https://doi.org/10.3390/pr10102027.
68. Yang, Y., Liang, Y., Wang, G., Liu, L., Yuan, C., Yu, T., Li, Q., Zeng, F., Gu, G. Enhanced gas-sensing properties of the hierarchical TiO_2 hollow microspheres with exposed high-energy {001} crystal facets. *ACS Applied Materials & Interfaces*. 7 (2015) 24902–24908. https://doi.org/10.1021/acsami.5b08372.
69. Chang, J., Ahmad, M.Z., Wlodarski, W., Waclawik, E.R. Self-assembled 3D ZnO porous structures with exposed reactive {0001} facets and their enhanced gas sensitivity. *Sensors*. 13 (2013) 8460. https://doi.org/10.3390/s130708445.
70. Kaneti, Y.V., Yue, J., Jiang, X., Yu, A. Synthesis of ZnO nanoflakes with exposed $(10\bar{1}0)$ for enhanced gas sensing performance. *Journal of Physical Chemistry C*. 117 (2013) 13153–13162. https://doi.org/10.1021/jp404329q.
71. Su, D., Xie, X., Dou, S., Wang, G. CuO single crystal with exposed {001} facets - A highly efficient material for gas sensing and Li-ion battery applications. *Scientific Reports*. 4 (2014) 5753. https://doi.org/10.1038/srep05753.
72. Xue, Z., Cheng, Z., Xu, J., Xiang, Q., Wang, X., Xu, J. Controllable evolution of dual defect Zni and VO associate-rich ZnO nanodishes with (0001) exposed facet and its multiple sensitization effect for ethanol detection. *ACS Applied Materials & Interfaces*. 9 (2017) 41559–41567. https://doi.org/10.1021/acsami.7b13370.
73. Liu, F., Wang, X., Chen, X., Song, X., Tian, J., Cui, H. Porous ZnO ultrathin nanosheets with high specific surface areas and abundant oxygen vacancies for acetylacetone gas sensing. *ACS Applied Materials & Interfaces*. 11 (2019) 24757–24763. https://doi.org/10.1021/acsami.9b06701.
74. Cao, F., Li, C., Li, M., Li, H., Huang, X., Yang, B. Direct growth of Al-doped ZnO ultrathin nanosheets on electrode for ethanol gas sensor application. *Applied Surface Science*. 447 (2018) 173–181. https://doi.org/10.1016/j.apsusc.2018.03.217.
75. Xiao, J., Liu, P., Liang, Y., Li, H.B., Yang, G.W. Porous tungsten oxide nanoflakes for highly alcohol sensitive performance. *Nanoscale*. 4 (2012) 7078–7083. https://doi.org/10.1039/C2NR32078A.
76. Miao, J., Chen, C., Meng, L., Lin, Y.S. Self-assembled monolayer of metal oxide nanosheet and structure and gas-sensing property relationship. *ACS Sensors*. 4 (2019) 1279–1290. https://doi.org/10.1021/acssensors.9b00162.
77. Tang, L., Tan, J., Nong, H., Liu, B., Cheng, H. Chemical vapor deposition growth of two-dimensional compound materials: controllability, material quality, and growth mechanism. *Accounts of Materials Research*. 2 (2021) 36–47. https://doi.org/10.1021/accountsmr.0c00063.
78. Tang, W., Fan, W., Zhang, W., Yang, Z., Li, L., Wang, Z., Chiang, Y., Liu, Y., Deng, L., He, L. Wet/sonochemical synthesis of enzymatic two-dimensional MnO_2 nanosheets for synergistic catalysis-enhanced phototheranostics. *Advanced Materials*. 31 (2019) 1900401. https://doi.org/10.1002/adma.201900401.
79. Dang, W., Wang, W., Yang, Y., Wang, Y., Huang, J., Fang, X., Wu, L., Rong, Z., Chen, X., Li, X., Huang, L., Tang, X. One-step hydrothermal synthesis of 2D WO_3 nanoplates@ graphene nanocomposite with superior anode performance for Lithium ion battery. *Electrochimica Acta*. 313 (2019) 99–108. https://doi.org/10.1016/j.electacta.2019.04.184.

80. Tripuramallu, B.K., Das, S.K. Hydrothermal synthesis and structural characterization of metal organophosphonate oxide materials: Role of metal-oxo clusters in the self assembly of metal phosphonate architectures. *Crystal Growth & Design*. 13 (2013) 2426–2434. https://doi.org/10.1021/cg4001347.
81. Sun, Z., Liao, T., Dou, Y., Hwang, S.M., Park, M., Jiang, L., Kim, J.H., Dou, S.X. Generalized self-assembly of scalable two-dimensional transition metal oxide nanosheets. *Nature Communications*. 5 (2014) 3813. https://doi.org/10.1038/ncomms4813.
82. Mhlongo, G.H., Shingange, K., Tshabalala, Z.P., Dhonge, B.P., Mahmoud, F.A., Mwakikunga, B.W., Motaung, D.E. Room temperature ferromagnetism and gas sensing in ZnO nanostructures: Influence of intrinsic defects and Mn, Co, Cu doping. *Applied Surface Science*. 390 (2016) 804–815. https://doi.org/10.1016/j.apsusc.2016.08.138.
83. Shingange, K., Mhlongo, G.H., Motaung, D.E., Ntwaeaborwa, O.M. Tailoring the sensing properties of microwave-assisted grown ZnO nanorods: Effect of irradiation time on luminescence and magnetic behaviour. *Journal of Alloys and Compounds*. 657 (2016) 917–926. https://doi.org/10.1016/j.jallcom.2015.10.069.
84. Kumar, R., Mamta, Kumari, R., Singh, V.N. SnO_2-Based NO_2 gas sensor with outstanding sensing performance at room temperature. *Micromachines*. 14 (2023) 728. https://doi.org/10.3390/mi14040728.
85. Motsoeneng, R.G., Kortidis, I., Ray, S.S., Motaung, D.E. Designing SnO_2 nanostructure-based sensors with tailored selectivity toward propanol and ethanol vapors. *ACS Omega*. 4 (2019) 13696–13709. https://doi.org/10.1021/acsomega.9b01079.
86. Tian, X., Cui, X., Lai, T., Ren, J., Yang, Z., Xiao, M., Wang, B., Xiao, X., Wang, Y. Gas sensors based on TiO_2 nanostructured materials for the detection of hazardous gases: A review. *Nano Materials Science*. 3 (2021) 390–403. https://doi.org/10.1016/j.nanoms.2021.05.011.
87. Oosthuizen, D.N., Motaung, D.E., Strydom, A.M., Swart, H.C. Underpinning the interaction between NO_2 and CuO nanoplatelets at room temperature by tailoring synthesis reaction base and time. *ACS Omega*. 4 (2019) 18035–18048. https://doi.org/10.1021/acsomega.9b01882.
88. Mokoena, T.P., Swart, H.C., Hillie, K.T., Motaung, D.E. Colour tuning from violet to blue emission stimulated by various nickel oxide nanostructures: Influence of bias voltage towards volatile organic compounds vapours. *Applied Surface Science*. 542 (2021) 148634. https://doi.org/10.1016/j.apsusc.2020.148634.
89. Yang, S., Jiang, C., Wei, S. Gas sensing in 2D materials. *Applied Physics Reviews*. 4 (2017) 021304. https://doi.org/10.1063/1.4983310.
90. Hübner, M., Simion, C.E., Tomescu-Stănoiu, A., Pokhrel, S., Bârsan, N., Weimar, U. Influence of humidity on CO sensing with p-type CuO thick film gas sensors. *Sensors and Actuator B: Chemical*. 153 (2011) 347–353. https://doi.org/10.1016/j.snb.2010.10.046.
91. Zhang, L., Zhao, J., Lu, H., Li, L., Zheng, J., Li, H., Zhu, Z. Facile synthesis and ultrahigh ethanol response of hierarchically porous ZnO nanosheets. *Sensors and Actuators B: Chemical*. 161 (2012) 209–215. https://doi.org/10.1016/j.snb.2011.10.021.
92. Oosthuizen, D.N., Motaung, D.E., Swart, H.C. In depth study on the notable room-temperature NO_2 gas sensor based on CuO nanoplatelets prepared by sonochemical method: Comparison of various bases. *Sensors and Actuators B: Chemical*. 266 (2018) 761–772. https://doi.org/10.1016/j.snb.2018.03.106.
93. Zhao, J., Huang, X., Yin, Y., Liao, Y., Mo, H., Qian, Q., Guo, Y., Chen, X., Zhang, Z., Hua, M. Two-dimensional gallium oxide monolayer for gas-sensing application. *The Journal of Physical Chemistry Letters*. 12 (2021) 5813–5820. https://doi.org/10.1021/acs.jpclett.1c01393.
94. Li, J., Wu, J., Yu, Y. DFT exploration of sensor performances of two-dimensional WO_3 to ten small gases in terms of work function and band gap changes and I-V responses. *Applied Surface Science*. 546 (2021) 149104. https://doi.org/10.1016/j.apsusc.2021.149104.
95. Qin, Y., Ding, W., Zhao, R. ZIF-8-derived ZnTi-LDHs with unique self-supported architecture and corresponding LDHs/rGO hybrid for gas sensor applications. *Chemical Physics Letters*. 781 (2021) 138965. https://doi.org/10.1016/j.cplett.2021.138965.
96. Sun, H., Chu, Z., Hong, D., Zhang, G., Xie, Y., Li, L., Shi, K. Three-dimensional hierarchical flower-like Mg–Al-layered double hydroxides: Fabrication, characterization and enhanced sensing properties to NO_x at room temperature. *Journal of Alloys and Compounds*. 658 (2016) 561–568. https://doi.org/10.1016/j.jallcom.2015.10.237.
97. Pacuła, A., Socha, R.P., Zimowska, M., Ruggiero-Mikołajczyk, M., Mucha, D., Nowak, P. Application of as-synthesized Co–Al layered double hydroxides for the preparation of the electroactive composites containing N-doped carbon nanotubes. *Applied Clay Science*. 72 (2013) 163–174. https://doi.org/10.1016/j.clay.2012.11.007.

98. Shingange, K., Swart, H.C., Mhlongo, G.H. $LaBO_3$ (B= Fe, Co) nanofibers and their structural, luminescence and gas sensing characteristics. *Physica B: Condensed Matter*. 578 (2020) 411883. https://doi.org/10.1016/j.physb.2019.411883.
99. Li, B., Osada, M., Ozawa, T.C., Sasaki, T. RbBiNb2O7: A new lead-free high-Tc ferroelectric. *Chemistry of Materials*. 24 (2012) 3111–3113.
100. Cao, D.H., Stoumpos, C.C., Farha, O.K., Hupp, J.T., Kanatzidis, M.G. 2D homologous perovskites as light-absorbing materials for solar cell applications. *Journal of the American Chemical Society*. 137 (2015) 7843–7850. https://doi.org/10.1021/jacs.5b03796.
101. Saparov, B., Mitzi, D.B. Organic–inorganic perovskites: Structural versatility for functional materials design. *Chemical Reviews*. 116 (2016) 4558–4596. https://doi.org/10.1021/acs.chemrev.5b00715.
102. Maheshwari, S., Savenije, T.J., Renaud, N., Grozema, F.C. Computational design of two-dimensional perovskites with functional organic cations. *The Journal of Physical Chemistry C*. 122 (2018) 17118–17122. https://doi.org/10.1021/acs.jpcc.8b05715.
103. Jiao, W., He, J., Zhang, L. Synthesis and high ammonia gas sensitivity of $(CH_3NH_3)PbBr_{3-x}I_x$ perovskite thin film at room temperature. *Sensors and Actuators B: Chemical*. 309 (2020) 127786. https://doi.org/10.1016/j.snb.2020.127786.
104. Maity, A., Mitra, S., Das, C., Siraj, S., Raychaudhuri, A.K., Ghosh, B. Universal sensing of ammonia gas by family of lead halide perovskites based on paper sensors: Experiment and molecular dynamics. *Materials Research Bulletin*. 136 (2021) 111142. https://doi.org/10.1016/j.materresbull.2020.111142.
105. Hien, V.X., Hoat, P.D., Hung, P.T., Lee, S., Lee, J., Heo, Y. Room-temperature NO_2 sensor based on a hybrid nanomaterial of methylammonium tin iodide submicron spheres and tin dioxide nanowires. *Scripta Materialia*. 188 (2020) 107–111. https://doi.org/10.1016/j.scriptamat.2020.07.022.
106. Stoeckel, M., Gobbi, M., Bonacchi, S., Liscio, F., Ferlauto, L., Orgiu, E., Samorì, P. Reversible, fast, and wide-range oxygen sensor based on nanostructured organometal halide perovskite. *Advanced Materials*. 29 (2017) 1702469. https://doi.org/10.1002/adma.201702469.
107. Haque, M.A., Syed, A., Akhtar, F.H., Shevate, R., Singh, S., Peinemann, K., Baran, D., Wu, T. Giant humidity effect on hybrid halide perovskite microstripes: Reversibility and sensing mechanism. *ACS Applied Materials & Interfaces*. 11 (2019) 29821–29829. https://doi.org/10.1021/acsami.9b07751.
108. Lang, F., Shargaieva, O., Brus, V.V., Neitzert, H.C., Rappich, J., Nickel, N.H. Influence of radiation on the properties and the stability of hybrid perovskites. *Advanced Materials*. 30 (2018) 1702905. https://doi.org/https://doi.org/10.1002/adma.201702905.
109. Ponchai, J., Srathongsian, L., Amratisha, K., Boonthum, C., Sahasithiwat, S., Ruankham, P., Kanjanaboos, P. Modified colored semi-transparent perovskite solar cells with enhanced stability. *Journal of Alloys and Compounds*. 875 (2021) 159781. https://doi.org/10.1016/j.jallcom.2021.159781.
110. Parikh, N., Tavakoli, M.M., Pandey, M., Kumar, M., Prochowicz, D., Chavan, R.D., Yadav, P. Two-dimensional halide perovskite single crystals: principles and promises. *Emergent Materials*. 4 (2021) 865–880. https://doi.org/10.1007/s42247-021-00177-7.
111. Tien, C., Lee, K., Tao, C., Lin, Z., Lin, Z., Chen, L. Two-dimensional $(PEA)_2PbBr_4$ perovskites sensors for highly sensitive ethanol vapor detection. *Sensors*. 22 (2022) 8155. https://doi.org/10.3390/s22218155.
112. Chen, C., Cai, Q., Luo, F., Dong, N., Guo, L., Qiu, B., Lin, Z. Sensitive fluorescent sensor for hydrogen sulfide in rat brain microdialysis via $CsPbBr_3$ quantum dots. *Analytical Chemistry*. 91 (2019) 15915–15921. https://doi.org/10.1021/acs.analchem.9b04387.
113. Jariwala, D., Marks, T.J., Hersam, M.C. Mixed-dimensional van der Waals heterostructures. *Nature Materials*. 16 (2017) 170–181. https://doi.org/10.1038/nmat4703.
114. Liu, Y., Huang, Y., Duan, X. Van der Waals integration before and beyond two-dimensional materials. *Nature*. 567 (2019) 323–333. https://doi.org/10.1038/s41586-019-1013-x.
115. Boulesbaa, A., Wang, K., Mahjouri-Samani, M., Tian, M., Puretzky, A.A., Ivanov, I., Rouleau, C.M., Xiao, K., Sumpter, B.G., Geohegan, D.B. Ultrafast charge transfer and hybrid exciton formation in 2D/0D heterostructures. *Journal of the American Chemical Society*. 138 (2016) 14713–14719. https://doi.org/https://doi.org/10.1021/jacs.6b08883.
116. Sinha, S., Kim, H., Robertson, A.W. Preparation and application of 0D-2D nanomaterial hybrid heterostructures for energy applications. *Materials Today Advances*. 12 (2021) 100169. https://doi.org/10.1016/j.mtadv.2021.100169.
117. Wang, P., Jia, C., Huang, Y., Duan, X. Van der Waals heterostructures by design: from 1D and 2D to 3D. *Matter*. 4 (2021) 552–581. https://doi.org/10.1016/j.matt.2020.12.015.
118. Xue, S., Wu, G., Li, M., Liu, Z., Deng, Y., Han, W., Lv, X., Wan, S., Xi, X., Yang, D., Dong, A. Generalized assembly of sandwich-like 0D/2D/0D heterostructures with highly exposed surfaces toward superior electrochemical performances. *Nano Research*. 15 (2022) 255–263. https://doi.org/10.1007/s12274-021-3468-y.

119. Withers, F., Del Pozo-Zamudio, O., Mishchenko, A., Rooney, A.P., Gholinia, A., Watanabe, K., Taniguchi, T., Haigh, S.J., Geim, A.K., Tartakovskii, A.I., Novoselov, K.S. Light-emitting diodes by band-structure engineering in van der Waals heterostructures. *Nature Materials*. 14 (2015) 301–306. https://doi.org/10.1038/nmat4205.
120. Zhou, X., Hu, X., Yu, J., Liu, S., Shu, Z., Zhang, Q., Li, H., Ma, Y., Xu, H., Zhai, T. 2D layered material-based van der Waals heterostructures for optoelectronics. *Advanced Functional Materials*. 28 (2018) 1706587. https://doi.org/10.1002/adfm.201706587.
121. Ruzmetov, D., Zhang, K., Stan, G., Kalanyan, B., Bhimanapati, G.R., Eichfeld, S.M., Burke, R.A., Shah, P.B., O'Regan, T.P., Crowne, F.J., Birdwell, A.G., Robinson, J.A., Davydov, A.V., Ivanov, T.G. Vertical 2D/3D semiconductor heterostructures based on epitaxial molybdenum disulfide and gallium nitride. *ACS Nano*. 10 (2016) 3580–3588. https://doi.org/10.1021/acsnano.5b08008.
122. Joshi, N., Braunger, M.L., Shimizu, F.M., Riul Jr, A., Oliveira, O.N. Insights into nano-heterostructured materials for gas sensing: A review. *Multifunctional Materials*. 4 (2021) 032002. https://doi.org/10.1088/2399-7532/ac1732.
123. Singh, A., Sikarwar, S., Verma, A., Chandra Yadav, B. The recent development of metal oxide heterostructures based gas sensor, their future opportunities and challenges: A review. *Sensors and Actuators A: Physical*. 332 (2021) 113127. https://doi.org/10.1016/j.sna.2021.113127.
124. Yang, S., Lei, G., Xu, H., Lan, Z., Wang, Z., Gu, H. Metal oxide based heterojunctions for gas sensors: A review. *Nanomaterials*. 11 (2021) 1026. https://doi.org/10.3390/nano11041026.
125. Yang, S., Lei, G., Lan, Z., Xie, W., Yang, B., Xu, H., Wang, Z., Gu, H. Enhancement of the room-temperature hydrogen sensing performance of MoO_3 nanoribbons annealed in a reducing gas. *International Journal of Hydrogen Energy*. 44 (2019) 7725–7733. https://doi.org/10.1016/j.ijhydene.2019.01.205.
126. Zappa, D., Galstyan, V., Kaur, N., Munasinghe Arachchige, H.M.M., Sisman, O., Comini, E. "Metal oxide -based heterostructures for gas sensors"- A review. *Analytica Chimica Acta*. 1039 (2018) 1–23. https://doi.org/10.1016/j.aca.2018.09.020.
127. Li, Z., Li, H., Wu, Z., Wang, M., Luo, J., Torun, H., Hu, P., Yang, C., Grundmann, M., Liu, X. Advances in designs and mechanisms of semiconducting metal oxide nanostructures for high-precision gas sensors operated at room temperature. *Materials Horizons*. 6 (2019) 470–506. https://doi.org/https://doi.org/10.1039/C8MH01365A.
128. Ju, D., Xu, H., Qiu, Z., Guo, J., Zhang, J., Cao, B. Highly sensitive and selective triethylamine-sensing properties of nanosheets directly grown on ceramic tube by forming NiO/ZnO PN heterojunction. *Sensors and Actuators B: Chemical*. 200 (2014) 288–296. https://doi.org/10.1016/j.snb.2014.04.029.
129. Yang, X., Shi, Y., Gong, F., Chen, J., Jin, G., Guo, Q., Zhang, H., Zhang, Y. Asymmetric interfacial oxygen sites of porous CeO_2-SnO_2 nanosheets enabling highly sensitive and selective detection of 3-hydroxy-2-butanone biomarkers. *Sensors and Actuators B: Chemical*. 371 (2022) 132500. https://doi.org/10.1016/j.snb.2022.132500.
130. Gao, X., Ouyang, Q., Zhu, C., Zhang, X., Chen, Y. Porous MoO_3/SnO_2 nanoflakes with n–n junctions for sensing H_2S. *ACS Applied Nano Materials*. 2 (2019) 2418–2425. https://doi.org/10.1021/acsanm.9b00308.
131. Yuan, K., Zhu, L., Yang, J., Hang, C., Tao, J., Ma, H., Jiang, A., Zhang, D.W., Lu, H. Precise preparation of WO_3@SnO_2 core shell nanosheets for efficient NH_3 gas sensing. *Journal of Colloid and Interface Science*. 568 (2020) 81–88. https://doi.org/10.1016/j.jcis.2020.02.042.
132. Yan, S., Liang, X., Song, H., Ma, S., Lu, Y. Synthesis of porous CeO_2-SnO_2 nanosheets gas sensors with enhanced sensitivity. *Ceramics International*. 44 (2018) 358–363. https://doi.org/10.1016/j.ceramint.2017.09.181.
133. Xu, H., Ju, J., Li, W., Zhang, J., Wang, J., Cao, B. Superior triethylamine-sensing properties based on TiO_2/SnO_2 n–n heterojunction nanosheets directly grown on ceramic tubes. *Sensors and Actuators B: Chemical*. 228 (2016) 634–642. https://doi.org/10.1016/j.snb.2016.01.059.
134. Wang, Y., Qu, F., Liu, J., Wang, Y., Zhou, J., Ruan, S. Enhanced H_2S sensing characteristics of CuO-NiO core-shell microspheres sensors. *Sensors and Actuators B: Chemical*. 209 (2015) 515–523. https://doi.org/10.1016/j.snb.2014.12.010.
135. Sik Choi, M., Young Kim, M., Mirzaei, A., Kim, H., Kim, S., Baek, S., Won Chun, D., Jin, C., Hyoung Lee, K. Selective, sensitive, and stable NO_2 gas sensor based on porous ZnO nanosheets. *Applied Surface Science*. 568 (2021) 150910. https://doi.org/10.1016/j.apsusc.2021.150910.
136. Wang, X., Su, J., Chen, H., Li, G., Shi, Z., Zou, H., Zou, X. Ultrathin In_2O_3 nanosheets with uniform mesopores for highly sensitive nitric oxide detection. *ACS Applied Materials & Interfaces*. 9 (2017) 16335–16342. https://doi.org/10.1021/acsami.7b04395.
137. Ji, F., Ren, X., Zheng, X., Liu, Y., Pang, L., Jiang, J., Liu, S. 2D-MoO_3 nanosheets for superior gas sensors. *Nanoscale*. 8 (2016) 8696–8703. https://doi.org/10.1039/C6NR00880A.

138. Xiao, R., Wang, T., Feng, S., Zhang, X., Cheng, X., Gao, R., Huo, L., Gao, S., Xu, Y. Porous MoO_3 nanosheets for conductometric gas sensors to detect diisopropylamine. *Sensors and Actuators B: Chemical*. 382 (2023) 133472. https://doi.org/10.1016/j.snb.2023.133472.
139. Wang, M., Wang, Y., Li, X., Ge, C., Hussain, S., Liu, G., Qiao, G. WO_3 porous nanosheet arrays with enhanced low temperature NO_2 gas sensing performance. *Sensors and Actuators B: Chemical*. 316 (2020) 128050. https://doi.org/10.1016/j.snb.2020.128050.
140. Hoa, N.D., El-Safty, S.A. Synthesis of mesoporous NiO nanosheets for the detection of toxic NO_2 gas. *Chemistry – A European Journal*. 17 (2011) 12896–12901. https://doi.org/https://doi.org/10.1002/chem.201101122.
141. Feng, S., Yu, H., Zhang, X., Huo, L., Gao, R., Wang, P., Cheng, X., Major, Z., Gao, S., Xu, Y. Ionic liquid-assisted synthesis of 2D porous lotus root slice-shaped NiO nanomaterials for selective and highly sensitive detection of N_2H_4. *Sensors Actuators B: Chemical*. 359 (2022) 131529. https://doi.org/10.1016/j.snb.2022.131529.
142. Zhang, Z., Wen, Z., Ye, Z., Zhu, L. Gas sensors based on ultrathin porous Co_3O_4 nanosheets to detect acetone at low temperature. *RSC Advances*. 5 (2015) 59976–59982. https://doi.org/10.1039/C5RA08536E.
143. Xu, K., Zou, J., Tian, S., Yang, Y., Zeng, F., Yu, T., Zhang, Y., Jie, X., Yuan, C. Single-crystalline porous nanosheets assembled hierarchical Co_3O_4 microspheres for enhanced gas-sensing properties to trace xylene. *Sensors and Actuators B: Chemical*. 246 (2017) 68–77. https://doi.org/10.1016/j.snb.2017.02.071.
144. Qin, W., Yuan, Z., Gao, H., Zhang, R., Meng, F. Perovskite-structured $LaCoO_3$ modified ZnO gas sensor and investigation on its gas sensing mechanism by first principle. *Sensors and Actuators B: Chemical*. 341 (2021) 130015. https://doi.org/10.1016/j.snb.2021.130015.
145. Qin, Y., Gui, H., Ding, W. Enhance methanol-sensing properties based on Ag functionalized monolayer LDH nanosheet: A combined experimental and theoretical calculation investigation. *Physica E: Low-Dimensional Systems and Nanostructures*. 144 (2022) 115409. https://doi.org/10.1016/j.physe.2022.115409.
146. Wang, D., Yang, J., Bao, L., Cheng, Y., Tian, L., Ma, Q., Xu, J., Li, H., Wang, X. Pd nanocrystal sensitization two-dimension porous TiO_2 for instantaneous and high efficient H_2 detection. *Journal of Colloid and Interface Science*. 597 (2021) 29–38. https://doi.org/10.1016/j.jcis.2021.03.107.
147. Hao, Q., Liu, T., Liu, J., Liu, Q., Jing, X., Zhang, H., Huang, G., Wang, J. Controllable synthesis and enhanced gas sensing properties of a single-crystalline WO_3–rGO porous nanocomposite. *RSC Advances*. 7 (2017) 14192–14199. https://doi.org/10.1039/C6RA28379A.
148. Zhang, J., Zhang, K., Liu, S., Liang, X., Zhang, M. Reasonable construction of 2D porous NiO/Co_3O_4 nanosheets for efficient detection of xylene. *Sensors and Actuators B: Chemical*. 377 (2023) 133002. https://doi.org/10.1016/j.snb.2022.133002.
149. Qin, S., Tang, P., Feng, Y., Li, D. Novel ultrathin mesoporous ZnO-SnO_2 n-n heterojunction nanosheets with high sensitivity to ethanol. *Sensors and Actuators B: Chemical*. 309 (2020) 127801. https://doi.org/10.1016/j.snb.2020.127801.
150. Hui, G., Zhu, M., Yang, X., Liu, J., Pan, G., Wang, Z. Highly sensitive ethanol gas sensor based on CeO_2/ZnO binary heterojunction composite. *Materials Letters*. 278 (2020) 128453. https://doi.org/10.1016/j.matlet.2020.128453.
151. Xiong, Y., Liu, W., Wu, K., Liu, T., Chen, Y., Wang, X., Tian, J. Constructing ultrathin defective Co_3O_4/MoS_2 nanosheets based 2D/2D heterojunction toward room temperature NH_3 detection. *Journal of Alloys and Compounds*. 927 (2022) 166962. https://doi.org/10.1016/j.jallcom.2022.166962.
152. Xiao, Y., Hu, S., Liu, Y., Zhang, A., Yao, Z., Tian, Y., Li, H., Ning, Y., Li, F., Qu, F., Yao, D., Zhang, H. Pt-modified $BiVO_4$ nanosheets for enhanced acetone sensing. *Sensors and Actuators B: Chemical*. 389 (2023) 133853. https://doi.org/10.1016/j.snb.2023.133853.